Solar Energy 263 (2023) 111931

Contents lists available at ScienceDirect

Solar Energy

journal homepage: www.elsevier.com/locate/solener

An experimental study on hybrid control of a solar tracking system to maximize energy harvesting in Jordan

Ahmad Al-Othman [a], Tariq Younes [a], Ibrahim Al-Adwan [a], Mohammad Al Khawaldah [a], Hamza Alauthman [b,*], Mohammad Alkhedher [c], Mohamad Ramadan [d,e]

[a] Department of Mechatronics Engineering, Faculty of Engineering Technology, Al-Balqa Applied University, 100190 Amman, Jordan
[b] Department of Mechanical Engineering, Jordan University of Science and Technology, 10587 Irbid, Jordan
[c] Mechanical and Industrial Engineering Department, Abu Dhabi University, Abu Dhabi, UAE
[d] School of Engineering, International University of Beirut BIU, Beirut, Lebanon
[e] School of Engineering, Lebanese International University LIU, Bekaa, Lebanon

A R T I C L E I N F O

Keywords:
Solar tracking
Hybrid control
Searching path
Photovoltaic panels
Maximum power point tracking

A B S T R A C T

Due to its capacity to maximize the power produced by photovoltaic (PV) panels, solar tracking systems have grown in popularity. However, erratic weather conditions, like cloudy or overcast days, change the panel's preferred orientation. On sunny days, the panel is turned to face the sun's radiation; however, on cloudy or overcast days, diffused radiation alters the optimal position. This has increased the necessity for new search algorithms that control the orientation of the panel to generate the most power feasible regardless of the weather conditions. This study aims at developing a sun-tracking system that can adjust the solar panel's orientation to generate the maximum possible electrical output from solar energy in Jordan, regardless of the local climate. To achieve this; a hybrid controller has been created that combines an open-loop sun monitoring system with a dynamic feedback controller built on an active search algorithm. The suggested algorithm is built on the real-time measurement of the PV panels' waning solar irradiance by using small solar cell 0.6 W. The system switches to the recently proposed circular path finding method to locate the Maximum Power Point Tracking (MPPT) if the instantaneous irradiance level falls below a predetermined threshold (DNI irradiance). As a result of the testing phase, the generated power of a solar panel increased by about 35%, confirming the effectiveness of the newly proposed sun tracker hybrid control system. During experimental test, positive irradiance current noises are appeared, using average filter taking the mean of 100 values for one measurement.

1. Introduction

Due to the growing threat of global warming caused by increased energy consumption, it was necessary for countries to switch to clean and renewable energy sources in order to meet their energy demands. As a result of the development of renewable energy, renewable energy accounted for 11.9% of the world's primary energy in 2021 [1]. This appeared clearly with the increasing growth in investement in the renewable energy field, especially in the solar energy field; the achieved solar energy capacity reached to 100GW during 2012, and the number of countries installing more than 1 GW annually has increased to 18 [2]. However in 2022, the global capacity of installed photovoltaic (PV) exceeded of 1 TW, and the target of estimation, by 2050 the global capacity can be growth toward 75TW [3].

Jordan has begun investing significantly in renewable energy, particularly solar energy, as it receives direct solar radiation with an intensity of between 5 and 7 kWh/m^2; a daily average of 5.6 kWh/m^2 that falls on a horizontal surface [4]. In addition, Jordan's prime location on the sunbelt results in an annual irradiance between 1800 and 2700 kWh/m^2. This has prompted Jordan to adopt solar energy to reduce energy production costs resulting from traditional energy imports. In 2018, the government imported 8922 ktoe (1ktoe = 11,630,000 kWh), which equates to approximately 10% of Gross Domestic Product (GDP) [5]. This makes renewable energy an attractive

* Corresponding author.
E-mail addresses: 51715088001@std.bau.edu.jo (A. Al-Othman), tariqmog@bau.edu.jo (T. Younes), Ibrahim.aladwan@bau.edu.jo (I. Al-Adwan), m.alkhawaldah@bau.edu.jo (M. Al Khawaldah), hsalauthman19@eng.just.edu.jo (H. Alauthman), mohammad.alkhedher@adu.ac.ae (M. Alkhedher), mohamad.ramadan@liu.edu.lb (M. Ramadan).

https://doi.org/10.1016/j.solener.2023.111931
Received 22 May 2023; Received in revised form 23 July 2023; Accepted 1 August 2023
Available online 10 August 2023

Table 1
Summary of Solar tracking control systems.

Ref.	Control technique	Method limitations
[11]	• Dual-axis hybrid sun tracking system • There are two tracking systems: open-loop and closed-loop. • Searching motion: a square spiral path in the plane of azimuth and altitude. • 40–55% greater power generation than the open-loop method.	• Inability to detect the sun's location in the initial step, resulting in large deviations and increased search time. • Undefined irradiation threshold for activating the search procedure. • A minimal threshold that is not specified. • The time difference between real-time and ST causes the horizontal axis of ST to be misaligned with geographical north.
[27]	• Stationary multi-axis sun-tracking devices for the north, south, and east–west directions. • Based on the difference between photo sensors, follows the sun. • 30–45% more energy is generated than with a stationary PV system.	• System mainly describes the advantages of employing ST compared to fixed PV. • Cloudy days are not ideal for the system.
[23]	• Dual-axis solar tracking device. • Astronomical equations control a GPS module and digital compass sensor. • DAST produces 19 to 27% more energy than fixed-tilt PV panels.	• The home position of the azimuth axis is determined using GPS precision to calculate the geographical location and north magnetic direction. • The shadow and cloud effects are the system's primary downsides.
[20]	• Offline sensorless dual-axis sun tracker. • More solar energy was captured by 24.59%.	• The offline system is separated from any weather and external disturbance sensing feedback.
[21]	• The azimuth and zenith angles of the ST are modified based on the date and time. • Fuzzy controller to control motors speed. • Generated 35.6% more energy than a fixed panel system.	• The sensor-less DAST control system is more ideal for days with clear skies.
[31]	• Dual-axis hybrid sun tracking system: Open-loop system is regulated by an astronomical algorithm, while closed-loop system is controlled by four LDR sensors. • During the early hours of sunlight, the variable PV system is 23,3% more productive than the fixed PV system.	• The study implies a model with only two input parameters. • A yearly study is required to validate the system under various scenarios.

field for the studies and research required to develop solar technologies that increase energy production and efficiency. The solar industry has developed a multitude of sun-tracking technologies for PV power projects, which have increased energy gains in comparison to fixed PV solar power systems [6–8].

Earlier studies have examined the ability of sun trackers (ST) to increase collected energy by 23.23% compared to a stationary system [9]. Furthermore, some ST has the potential to reach 40% [10] when utilizing a more efficient sun tracker design, which plays a crucial role in boosting the amount of power captured by a PV panel. The heavy external disturbance caused by environmental factors such as dust and rain from heavy clouds [11,12] is one limitation of the energy collected by ST. On clear days, 85–90% of solar irradiation reaches the earth's surface directly, while 10 to 15% is lost through diffusion [13]. In contrast, cloudy days will diffuse solar irradiation on the cloud density or cloudiness level. Consequently, this emphasizes the significance of developing tracking strategies to increase the power produced by PV panels [14].

The purpose of this study is to improve the performance of dual-axis solar trackers (DAST) by adjusting the orientation of photovoltaic (PV) panels to capture the maximum amount of electrical power possible from solar energy. This work proposes a searching algorithm to control DAST's standalone 20 W PV panel; the methodology will consist of comparing two control systems: the first system is an open-loop system, which defines the sun angles based on time, date, and geographical location; the second system is controlled by a combination of a closed and an open-loop control strategy as a hybrid controller [15–17], using open-loop control and circular separability. Moreover, a MATLAB/Simulink simulation is used to determine the sun angles and predict the amount of power captured by the PV panel during the experimental period, taking into account the geographical location and date/time as a reference [18,19].

Sun tracking control systems have been the subject of numerous earlier investigations. In the field of passive sun tracker, [20] proposed offline sensorless DAST, which validated that using this method, 24.59 percent more solar energy was harvested yearly. The proposed system used a simple structure sun tracker compared with fixed PV with a lower manufacturing cost than sensor-based sun trackers, but which also tracks the sun more precisely. The vector of the sun is computed via the solar position algorithm. This technique resulted in a sun-tracking error of only 0.43°, which is smaller than the error of the sensorless and sensor-based DAST used.

However, [21] developed an intelligent control system for sun tracking where a fuzzy logic controller was used on a DC motor in DAST. A sensorless DAST was created that can change azimuth and zenith angles based on the date and time. This controller's inputs were errors and rate of change errors, and its output was the motors' speed. It was discovered that the proposed system's daily power output was 35.6 percent more than that of a fixed panel system.

Another study [22] built computer capabilities that boost the effectiveness of the tracking by using a fuzzy controller method. An electromechanical dual-axis PV tracker (azimuth and altitude) was designed and built by researchers to move the PV modules using two electrically driven motorized 36 DC motors. The actuators were managed by a sophisticated fuzzy Programmable Logic Controller (PLC), which moved the sun tracker. An experimental test that analyzes system performance and assesses the maximum radiation and electrical power for moving PV modules is being conducted in Amman, Jordan. The performance of a fixed PV system that is inclined at 32° towards the south and a dual-axis sun tracker are compared. The proposed technique increased daily electricity generation by more than 50% in the summer.

However, [23] created a portable DAST device that was controlled by astronomical equations. A Global Positioning System (GPS) module and a digital compass sensor determined the location for the tracking system. The altitude angle and azimuth angle were utilized to locate the sun in the sky depending on the day number (beginning with January 1) and time of day in order to make the PV panel perpendicular to solar radiation and to optimize electrical power generation. On a mostly clear day, the proposed tracking system produced 27% more energy than the fixed tilted PV panel. The proposed approach generates 19% more electricity than the fixed PV system during cloudy days. A Proportional Integral Derivative (PID) controller enhanced the precision of elevation and azimuth angles to 0.2° [23,24] by controlling the positioning system.

Numerous studies have looked into the possibilities of low-cost automatic dual-axis solar tracker systems. For instance, [25] developed a closed-loop active tracking system based on Light Dependent Resistor (LDR) sensors. A pseudo-azimuthal system with a digital logic design is used in the tracking method to enable easy rotation around the primary (north–south) and secondary (east–west) axes. The proposed tracking system demonstrated a notable gain in electrical energy

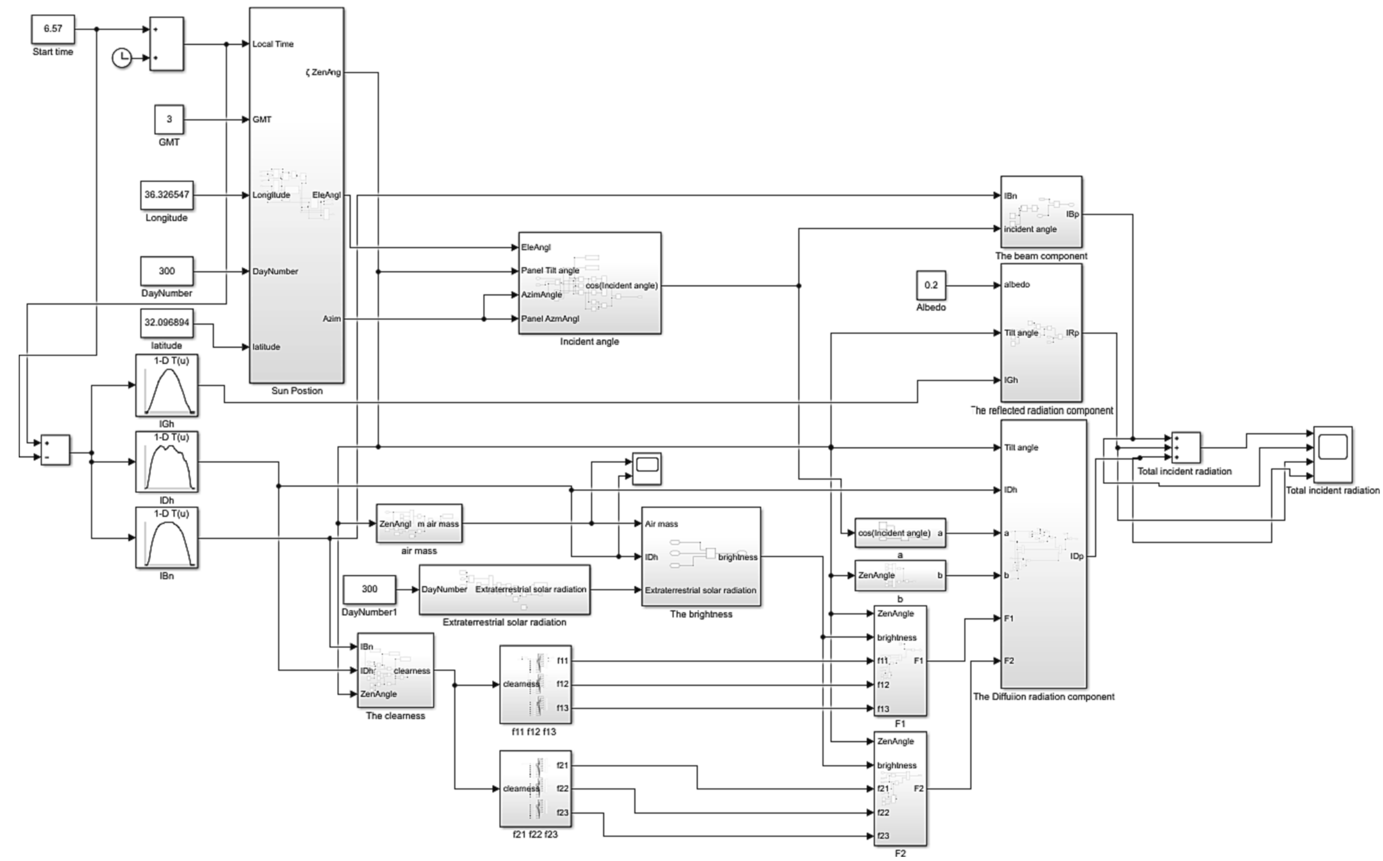

Fig. 1. Simulink model of total incident irradiation falling on dual-axis solar tracker for 26/10/2021.

efficiency, with an average increase of 44.89%, in an experimental comparison with a fixed flat-plate system.

A dual feedback control algorithm is proposed for a single-axis solar trackers of parabolic systems [26], this algorithm consists of using two feedbacks: photodiode solar sensors and shadow-based visual device to precise the position adjustment. This algorithm increased the stability and robustness of solar and decreased impact the disturbance of diffused radiation and nonlinearity of photodiode sensors.

Other studies have looked into multiple-axis sun-tracking systems in Jordan using stationary, east–west, and north–south processes. In order to track the sun based on the differences between the sensors, an electromechanical system controlled by optical sensors and Logo PLC was constructed. In comparison to the 32° slanted fixed PV cell, it was found that the multi-axis sun tracker increases output power by roughly 30–45% [27].

A systematic review presented of control algorithms for active solar tracking systems [28]. Authors classified these algorithms to three solar tracking control strategies: open-loop, closed-loop and hybrid-loop; combined open- and closed-loop. The review is shown that the advantages of hybrid-loop strategy are:

- the accuracy and precision of ST is high,
- ability of ST of working under cloudy conditions
- it's not need a continuous calibration.

An adaptive algorithm proposed to enhance the performance of dual-axis schedule tracker [29]. A practical method was proposed to determine the minimum value of solar energy collected by PV panel during a strong cloud scattering; by using power data of two mini PV panel. The developed dual-axis method of tracking the sun is 41% more efficient than the dual-axis schedule tracker.

Another author presents a development of DAST by using a Hybrid Controller [30], which is a novel combination astronomical equations-based open-loop control, a differential flatness based control over the movement of flat PV panel. The tracker is rotated by using linear actuators and using LDR array for real-time to adjustment the solar panel. This method increased the energy acquisition of ST by more than 25%.

In another proposed design of a hybrid controller for tracking system [31], the tracker is controlled by two strategies: the first is based on an open-loop astronomical algorithm, and the second is based on a simplified and intelligent controller (closed-loop). The astronomical algorithm (Solar Position Algorithm algorithm) that computes the sun vector components represented an open-loop controller. In contrast, the closed-loop controller used stepper motors to reduce the sun position error based on a normalized system error between open-loop angles and sun sensors (four LDR sensors). Using the MATLAB/ Simulink software suite, the system was implemented and executed. Early in the day, the suggested hybrid Solar Tracker System (STS) produced 23.3% more energy than the stationary PV system.

Another study has concentrated on the development of a control system that can improve the solar tracker for flat panels. To achieve this objective, the control system must design the ST's orientation with regard to the sun vector. The sun vector SQ(γ_s, α_s) represents the azimuth and elevation of the sun relative to the tracker's geographical location [32]. Stability and precision are two of the most important design considerations for the solar tracker. The ST is controlled by different control systems, including open-loop control systems [33,34], closed-loop control systems [35,36], and in certain situations, a mix of the two.

Another proposed hybrid control strategy consists of two feedbacks; an image processing and photosensor [37]. The image feedback using for avoiding disturbance of wind and clouds, however photosensors were used for precise control of solar tracker. The image-based control system operated as a backup for the photosensor-based control mechanism when cloudy conditions persisted for less than 20 min, and the

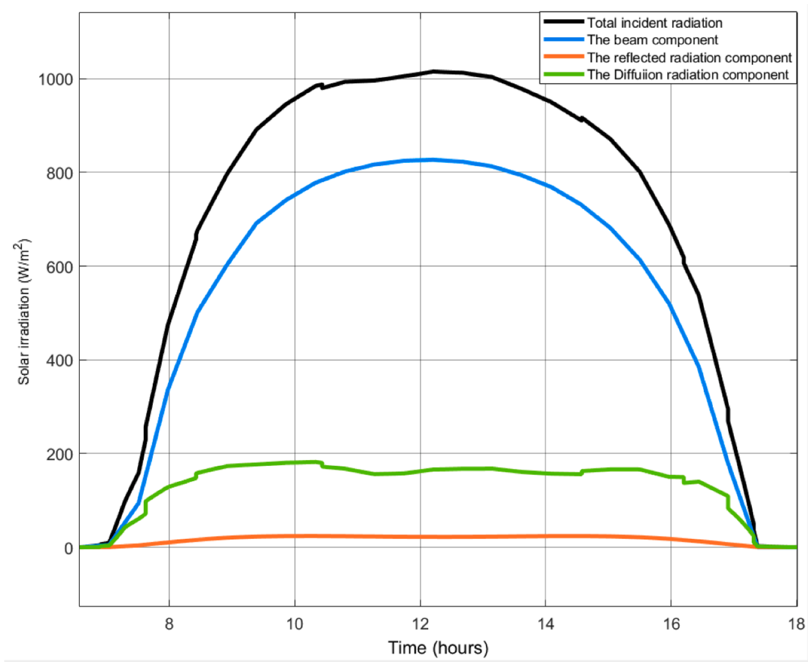

(a)

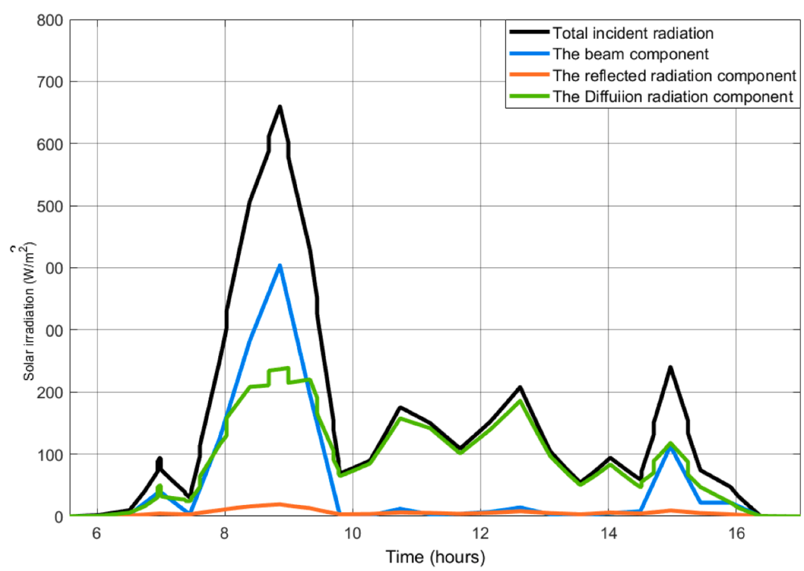

(b)

Fig. 2. Total incident irradiation on dual-axis tracker, (a) 26/10/2021 where the maximum irradiation was 1015.5 W/m^2 at 12:12:36, and (b) 31/10/2021 where the maximum irradiation was 659.7 W/m^2 at 8:51.

feedback generating by photosensors (S1 through S5). When the cloudy condition persisted for more than 20 min but less than three hours; the real-time video streaming system starts producing a signal to drive the stepper motors. When the sun image moved out of the camera frame; the position of solar tracker position is adjusted by Photosensors S6 and S7, in the statement of heavy clouds for a long time; the solar tracker was put in standby mode.

A hybrid control system combines an open-loop control system with a closed-loop control system [31]. Open-loop ST controllers are sometimes referred to as passive controllers. This controller uses astronomical formulae to steer photovoltaic panels towards the sun [23]. Active controller describes the closed-loop controller that tracks the sun's position using light-sensitive sensors [38] and an image processing system [39]. Table 1 shows a summary of solar tracking control systems used in the literature.

Numerous research have examined the path planning patterns utilized by solar tracking systems. Employing a dark-field imaging system to study micron-sized surface flaws. [40] were introduced three types of scanning path patterns: zigzag scanning path, contour parallel scanning path, and fractal scanning path. Time of scanning was the main drawback of these scanning types. In the study of path planning patterns, based on one mobile reference node to localize random static unknown nodes in the searching space [41], suggested in 2020 using scanning path correction and target tracking to evaluate surface defects. For the purpose of scanning a vast region, they devised a scanning path comprised of concentric circles with a circular outline. During testing of

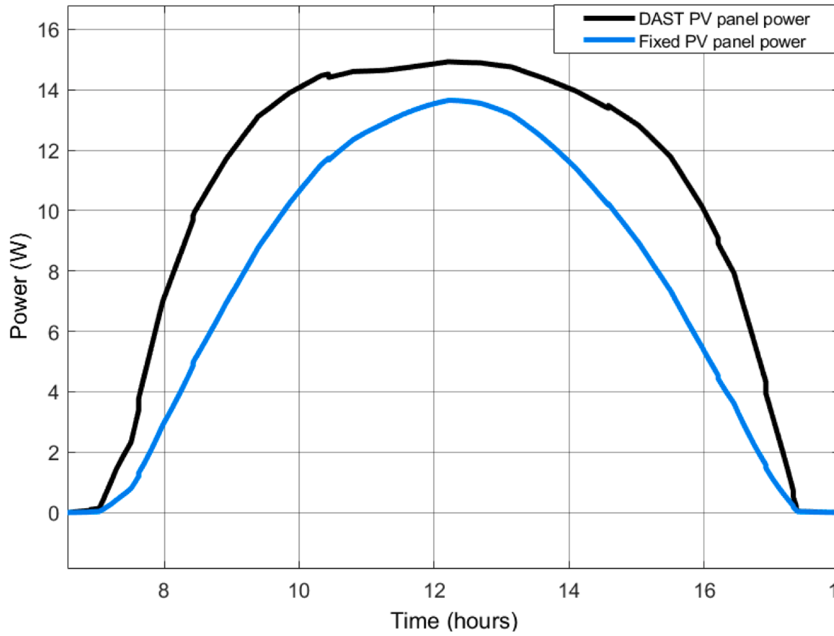

(a)

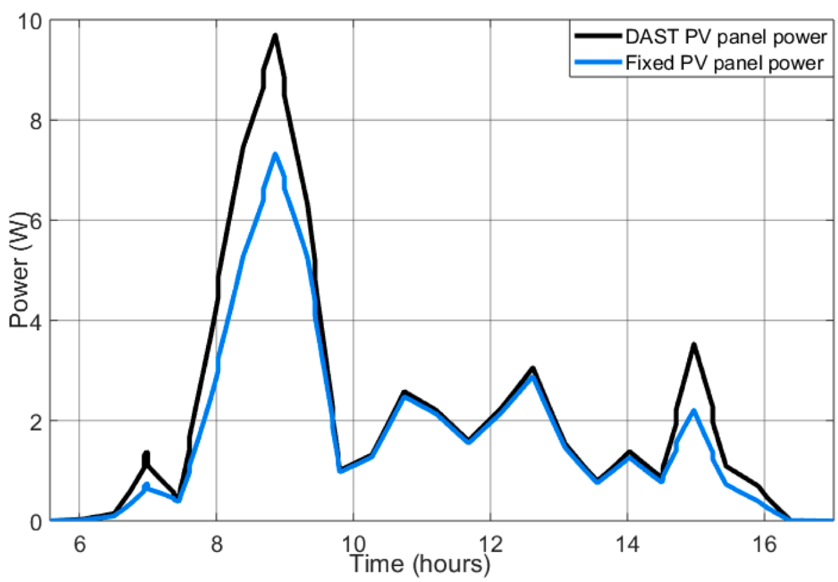

(b)

Fig. 3. The simulated output power for dual-axis tracker and fixed panel tilted at 23°, (a) 26/10/2021 where the maximum power was 14.9 W and 13.6 W at 12:12:36 respectively, and (b) 31/10/2021 where the maximum power was 9.7 W and 7.3 W at 8:51 respectively.

Table 2
PV panel technical data.

Peak Power Watt (Pmax)	20 W
Short-circuit current (I_{sc})	1.27 A
Open-circuit voltage (V_{oc})	21.44 V
Temperature coefficient of I_{sc} (K_i)	0.50 ±0.02%/°C
Temperature coefficient of V_{oc} (K_v)	−0.35 ±0.01%/°C
Series Resistance (R_s)	1.0547 Ω
Shunt Resistance (R_{sh})	405.962 Ω
Number of cells in series (N_s)	36
Diode ideality factor (A)	1.3
Efficiency	12.25%

the inspection system, 118 out of 120 existing faults were found. Consequently, the results demonstrate the usefulness of this strategy in raising the number of observable surface flaws. In the suggested scanning method, the precise location of the target is not provided; hence, the search region will be very vast based on the surrounding environmental conditions, which will impact experiment tracking.

[42] has implemented seven pre-designed searching trajectories: Random Wireless Positioning (RWP), Circle, Localization algorithm with a Mobile Anchor node based on Trilateration (LMAT), H-curve, Z-curve, Horizontal-Vertical (H–V) Scan and Diagonal trajectory. In comparison to other approaches, the circle finding path method has the shortest length and uses the least time and energy. Finding the quickest and least energy-intensive search strategy involves taking into account a

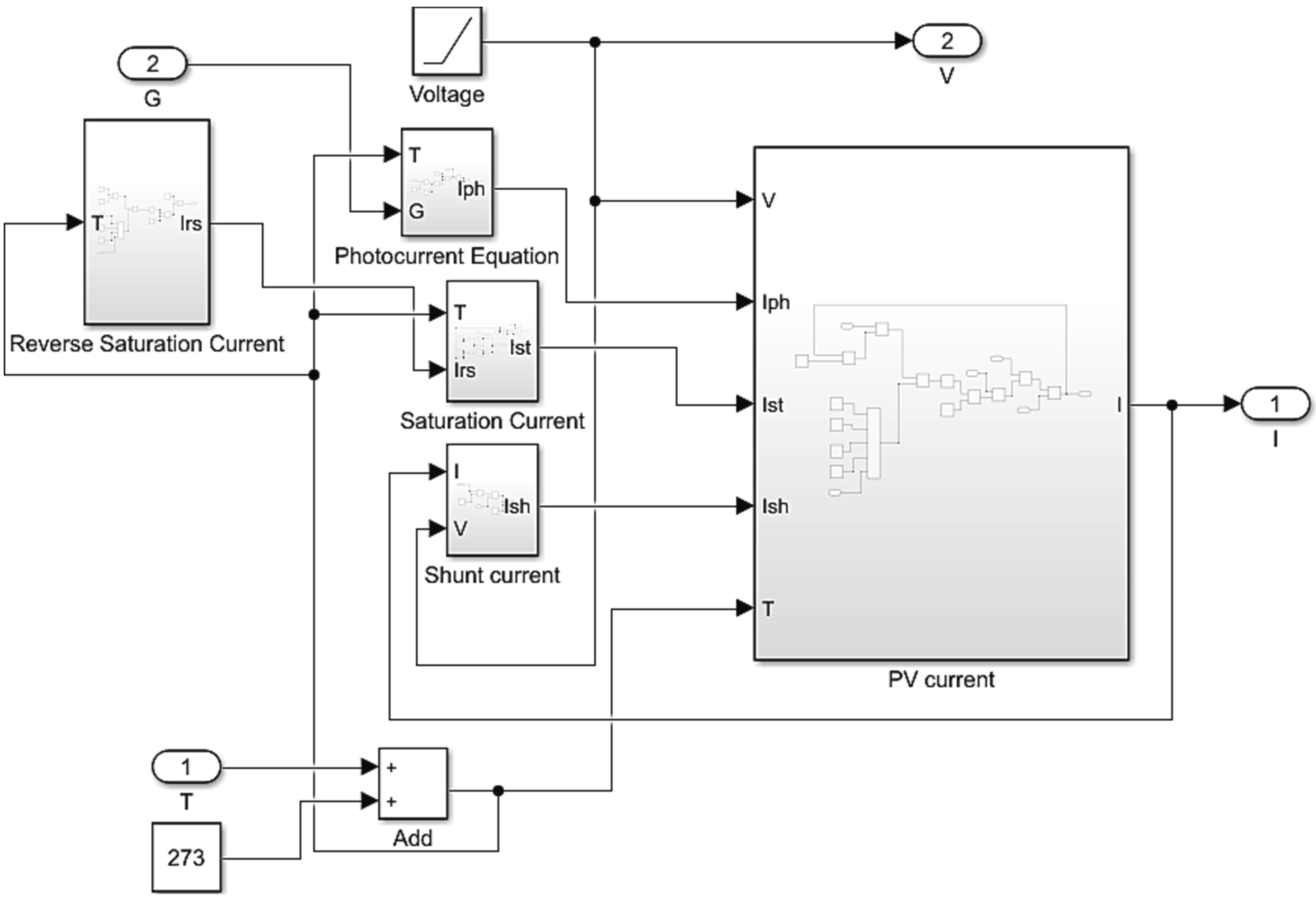

Fig. 4. PV panel simulation using Simulink.

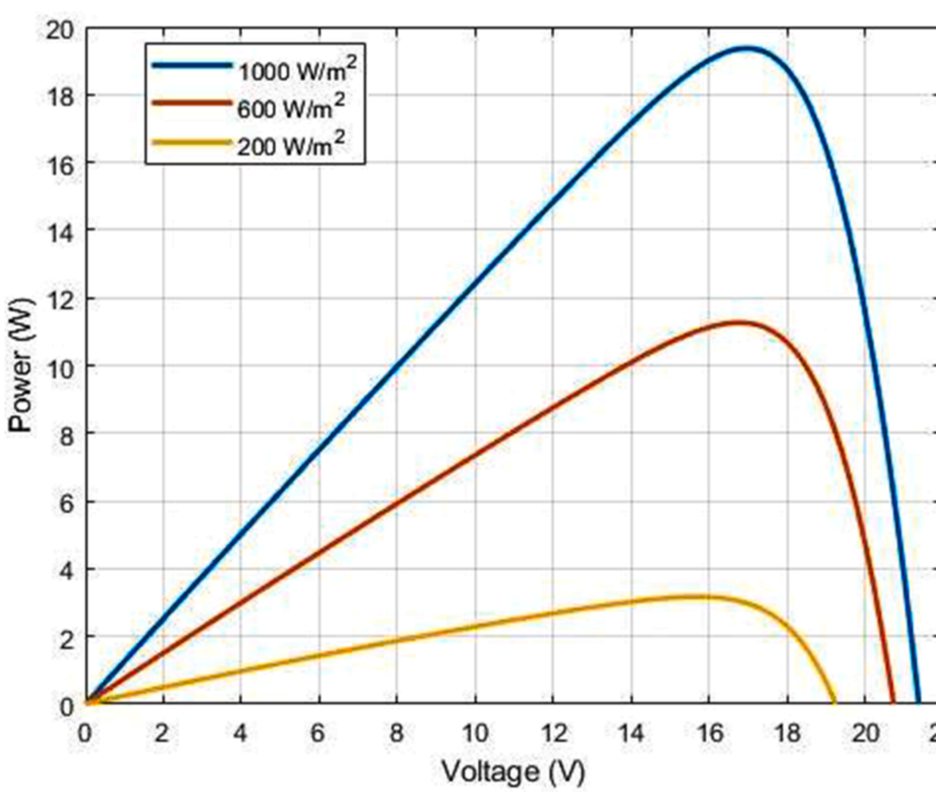

Fig. 5. P-V characteristics for PV panel with different irradiation values at 25 °C.

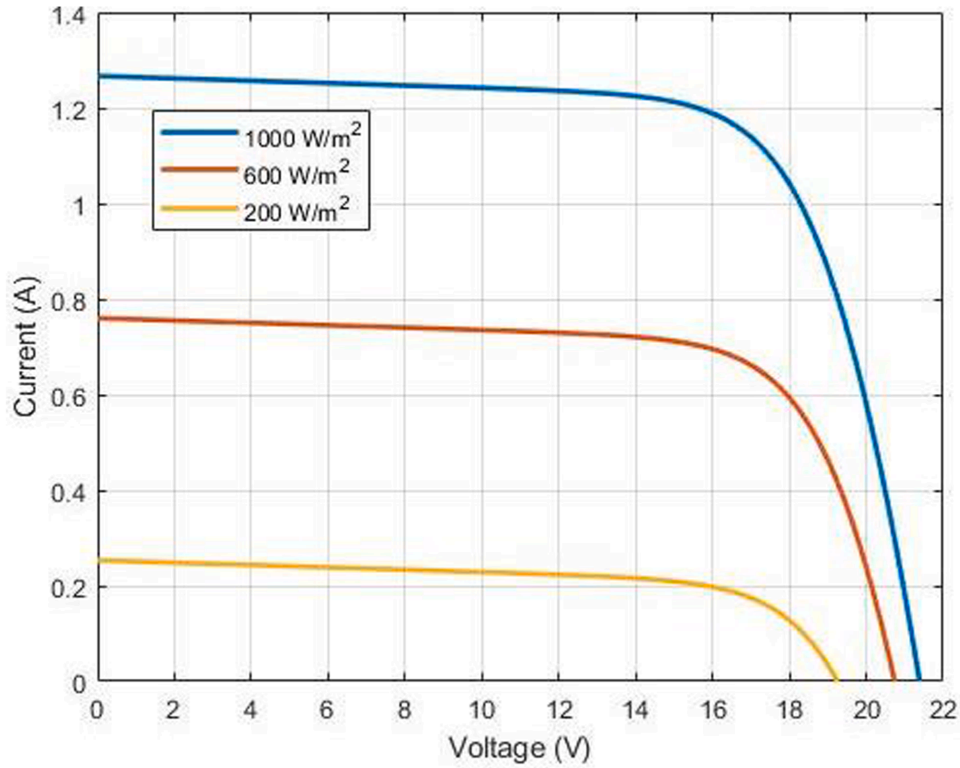

Fig. 6. I-V characteristics for PV panel with different irradiation values at 25 °C.

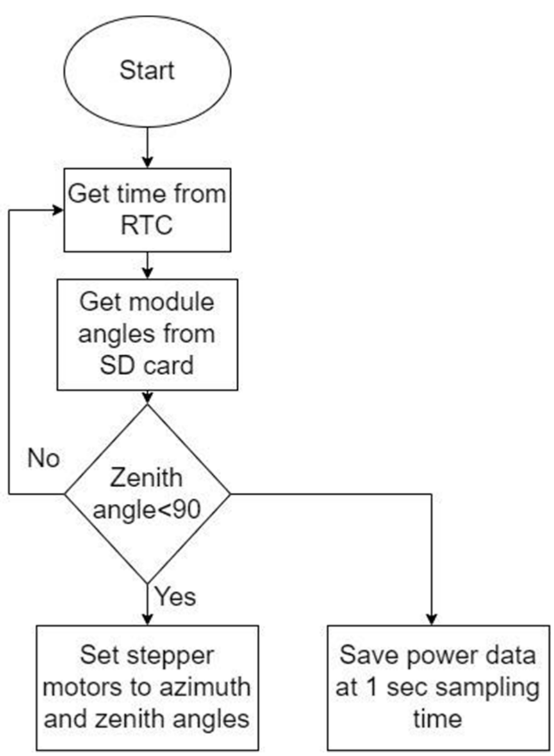

Fig. 7. Simplified flow chart of the open-loop system.

variety of searching behaviors to identify and locate the higher power point in the solar tracker's search area.

Two tracking methods were used in a control application of a DAST for solar tracking: an open-loop tracking strategy that operates in clear skies and is based on solar movement models, and a closed-loop tracking strategy that operates in cloudy skies and is based on power sensing [11]. A spiral square pattern in the azimuth-altitude plane represents the structure's searching motion, ST rotates in the pattern until detected the optimal location. From the experimental results, during 4 h of the day the electrical generated power of the hybrid system was 55% higher than the open-loop system. However, there was an offset in the timing between real-time and ST time, and a misalignment between ST horizontal axis and geographical north. This increased the level of uncertainty in the result collected by experiments. It is important to check the homing position of the ST at the beginning of each experiment.

This research aims to produce a hybrid open/closed-loop system with a proposed searching algorithm to generate maximum output electrical power. The contribution can be summarized as following points:

- The threshold at which the system is switched from open loop to searching mode is selected. The proposed system uses the direct normal irradiation values measured for a clear day in each month as a threshold level.
- If the instantaneous measured irradiation is less than this threshold, the system automatically switches to searching mode.
- To enhance the searching algorithm, a new criterion is developed to relate the circular search radius with instantaneous irradiation
- To guarantee the effectiveness of the proposed ST system, the homing position was ensured before each experiment.

Three main factors will be considered in the ST design in this study:

1. The sun's position: to define the sun vector SQ (γ_s, α_s) from the location of the ST system.
2. The control inputs: astronomical algorithm of the sun's position, power reading, geographical location, and time.

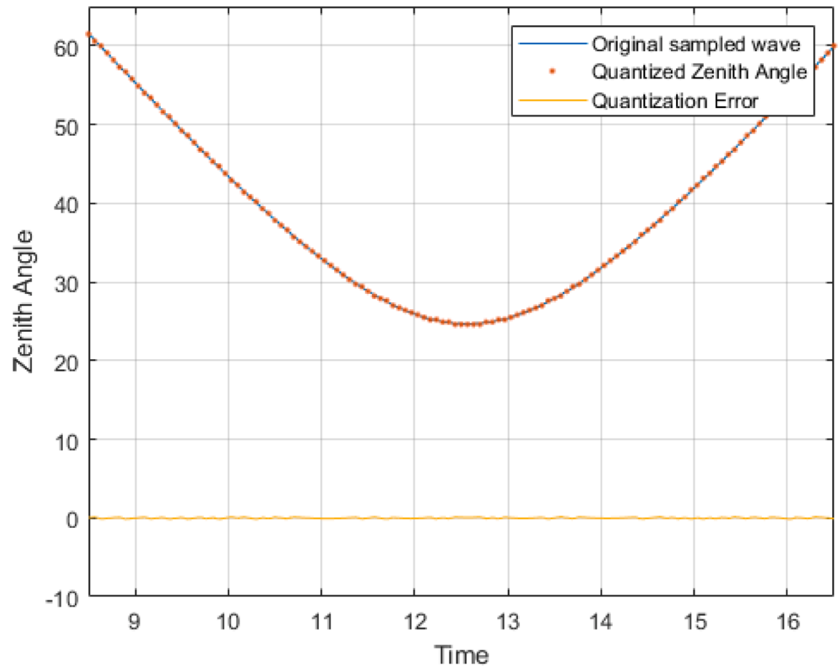

(a)

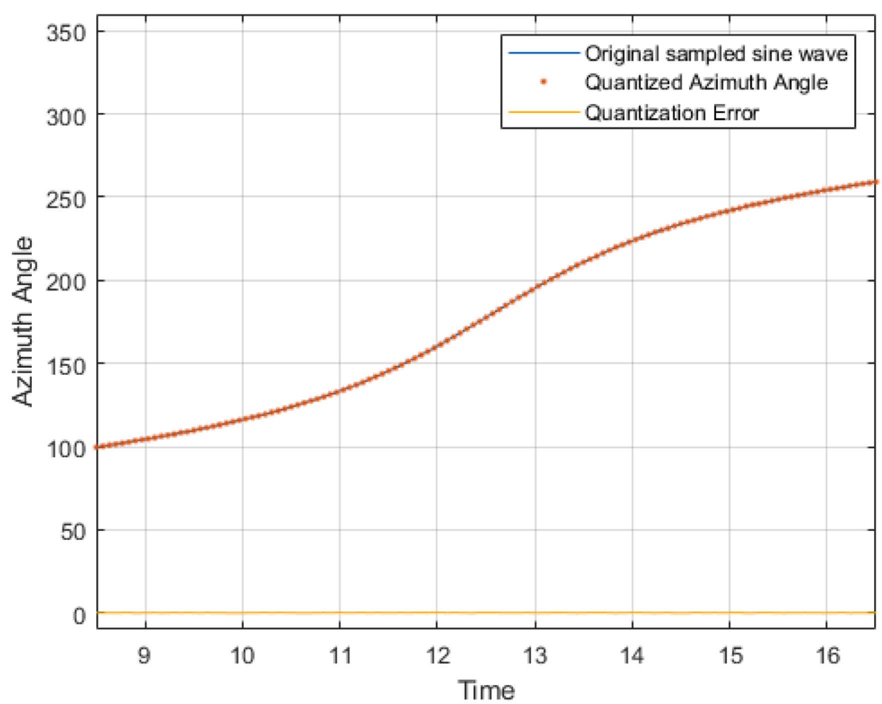

(b)

Fig. 8. (a) Zenith Angle and (b) Azimuth Angle of Module after quantization sampled for T = 4 min.

3. The control system: control flow and intelligence (state diagrams) to control the electric motors to move the PV panel towards the sun.

2. Modeling and simulation of solar tracker system

2.1. Modeling of total incident irradiation falling on dual-axis solar tracker

The Perez model, which has fewer prediction errors and is more accurate and dependable compared to other models [43], was used to create the total solar irradiation model using the MATLAB/Simulink

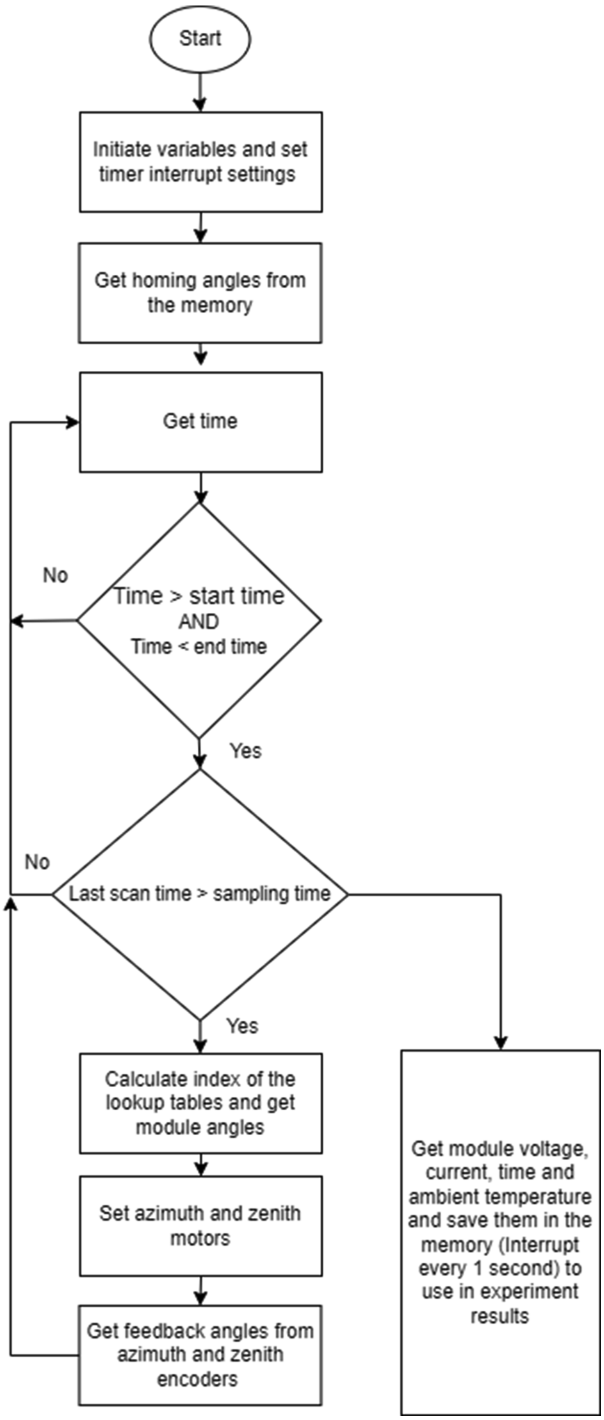

Fig. 9. Flow chart of DAST open-loop control system.

environment for a dual-axis tracker. The major database gives the horizontal irradiance values during the day (GHI, DNI, DHI), divided by 30-minute time intervals, taking into account geographic location, time, and day of the year, which are taken from Solacast data base website [44]. The Simulink model of total incident radiation falling on a dual-axis system on October 26, 2021, is depicted in Fig. 1.

Fig. 2 compares the total incident radiance for the two days, October 26 and October 31. Figure (2 a) depicts a stable irradiation value for a clear day, reaching its maximum value of 1015.5 W/m^2 at 12:33 (+3 GMT), while Fig. 2(b) depicts a variable irradiation value for a cloudy day, reaching its maximum value of 626.8 W/m^2 at 8:56 (+2 GMT). When there are thick cloud periods, the beam value is roughly zero, as seen in Fig. 2(b).

The relationship between the output power of PV panel and solar irradiation can be expressed in (1) [45]:

$$P = \eta_p I A_p \tag{1}$$

Where P is the output power PV panel [W], η_p is the PV efficiency [%], I is the total incident radiation [W/m^2], and A_p is the surface area of the panel [m^2].

When comparing the output power of dual-axis trackers with fixed PV panels, it was found that the best average tilt angle for collecting the highest output power for a fixed panel is roughly local latitude minus 9° or 10° [46]. The study's position is at latitude 32°, so the fixed panel's slope angle will be set to 23° and its azimuth will be directed toward the earth's magnetic south. According to Fig. 3, while employing the dual-axis tracker, the output power value increased by 34.39% and 24.47%, respectively, for days 26 and 31 of October.

2.2. Modeling and simulation of PV panel and solar radiation

Using MATLAB Simulink, the mathematical model of a PV panel based on a single diode equivalent circuit is carried out [47]. The parameters are set based on Standard Test Conditions (STC), where the temperature is 298 K (25 °C) and the amount of sunlight is 1000 W/m^2. Table 2 is a list of the values for both parallel and series resistance.

Based on Kirchhoff's Current Law (KCL) the PV current equals:

$$I_{pv} = I_{ph} - I_d - I_{sh} \tag{2}$$

The photocurrent I_{ph} which depends on Temperature and Irradiance value, I_{ph} can be obtained by:

$$I_{ph} = [I_{SC} + K_i(T - T_{ref})]\left(\frac{G}{G_{ref}}\right) \tag{3}$$

Where I_{SC} is the short circuit current [A], K_i is the temperature coefficient of short circuit current [%/°C or %/Kelvin], T is the cell temperature of in [K], T_{ref} is the Standard temperature [298 k], G is the Solar irradiation in W/m^2, and G_{ref} is the STC irradiance [1000 W/m^2].

The reverse saturation current can be obtained as:

$$I_{rs} = \frac{I_{sc}}{e^{\frac{qV_{oc}}{N_s kAT}} - 1} \tag{4}$$

Where I_{rs} is the reverse saturation current [A], q is the electron charge [1.6×10^{-19} columb], V$_{oc}$ is the open circuit voltage [V], N_s is a cells number that connects in series, A is the diode ideality factor, and K is Boltzmann constant [1.3805×10^{-23}J/K].

The value of saturation current I_{st} depends on the temperature of the cell:

$$I_{st} = I_{rs}\left(\frac{T}{T_{ref}}\right)^3 .\exp\left(\frac{qE_{g0}\left(\frac{1}{T} - \frac{1}{T_{ref}}\right)}{K.}\right) \tag{5}$$

Where E_{g0} is the semiconductor band gap energy [1.1 eV].

The PV output current is:

$$I_{pv} = I_{ph} - I_{st}\left[\exp\left(\frac{V_{oc} + I_{pv}R_s}{AkTN_s}\right) - 1\right] - I_{sh} \tag{6}$$

Where I_{pv} is the output current of the cell, R_s is the series resistance, and V$_{oc}$ is the output voltage in volts.

The shunt current I_{sh} is equal to:

$$I_{sh} = \frac{V_{oc} + I_{pv}R_s}{R_{sh}} \tag{7}$$

Where R_{sh} is shunt resistance.

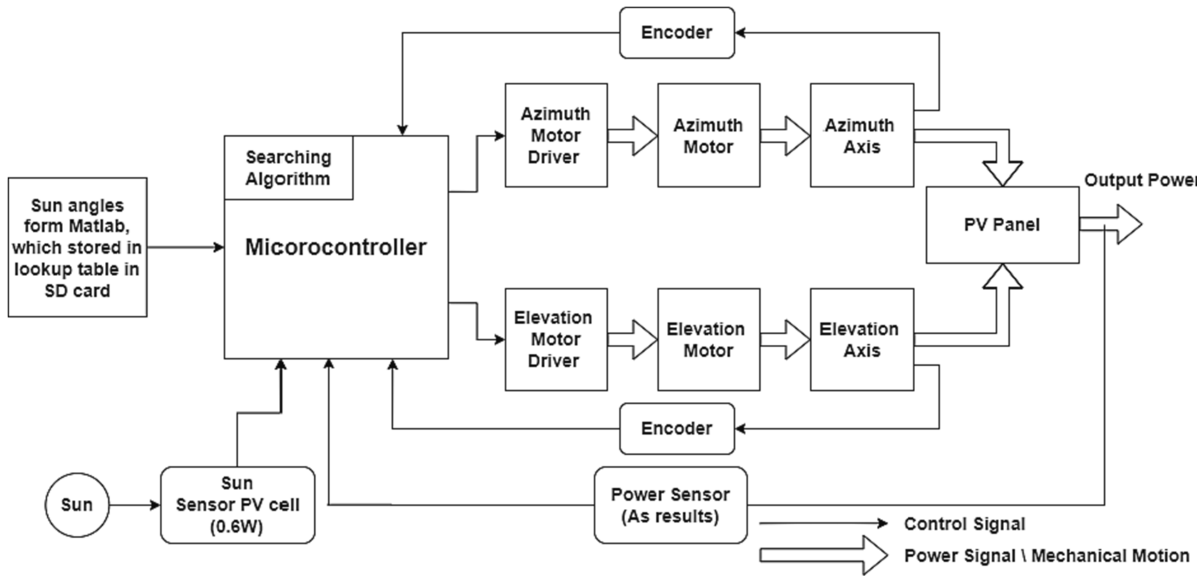

Fig. 10. Block diagram of closed-control system for the solar tracker.

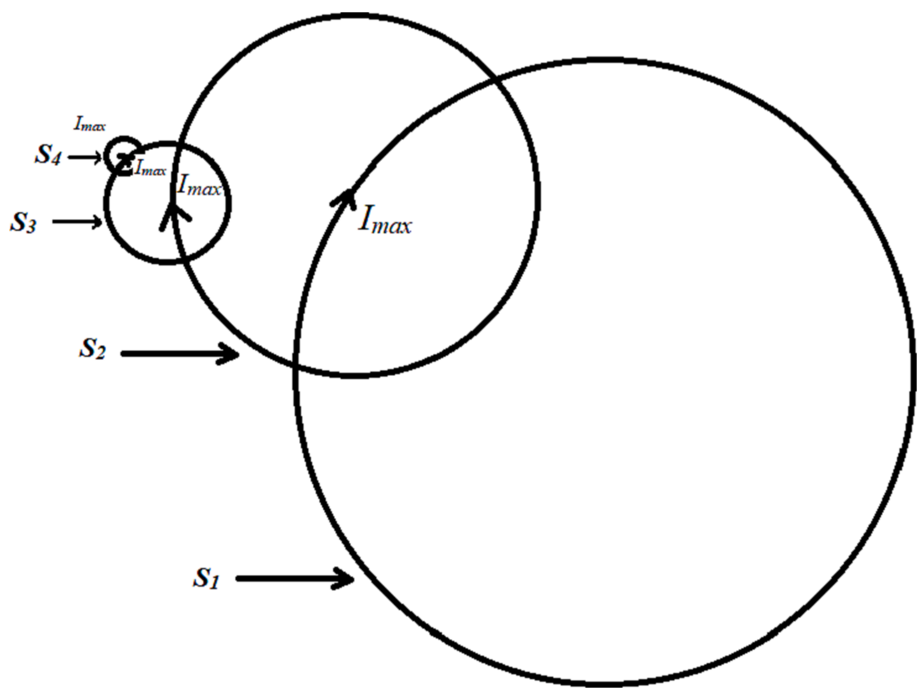

Fig. 11. Proposed circular searching algorithm.

Fig. 4 show the PV Simulink Implantation based on Eqs. (2)–(7).

As shown by the P-V characteristic with variable radiation at 25 °C (Fig. 5), the maximum output power of a PV panel increases as solar radiation increases. Fig. 6 demonstrates how an increase in solar radiation that strikes a PV panel induces a rise in short circuit current, which raises the panel's open circuit voltage [48].

3. Solar tracker controller system

It is crucial to establish the beginning positions (homing angles) for the azimuth and zenith axes because the solar tracker prototype is not stationary. The zero of each angle will be the homing angle. The rotating disk will be turned to align with the azimuth axis of the earth's axis of rotation.

The disk is rotated manually, a compass is used to align it, and the azimuth angle is set to zero. By relocating the solar carrier to be parallel to the horizon, the zenith angle will be set to zero. The spirit level will be used to do this. The homing functions are only employed during the first run or when the position of the portable solar tracker is altered.

3.1. Open-loop control system of the solar tracker

The implementation of this system, which uses time, date, and geographic latitude to determine azimuth and altitude angles, depends on Sun Position Algorithm (SPA). The solar tracker and the sun provide feedback to this control system. A simplified flow diagram of the open-loop system is shown in Fig. 7.

The values of the solar position (azimuth and zenith angles) and the

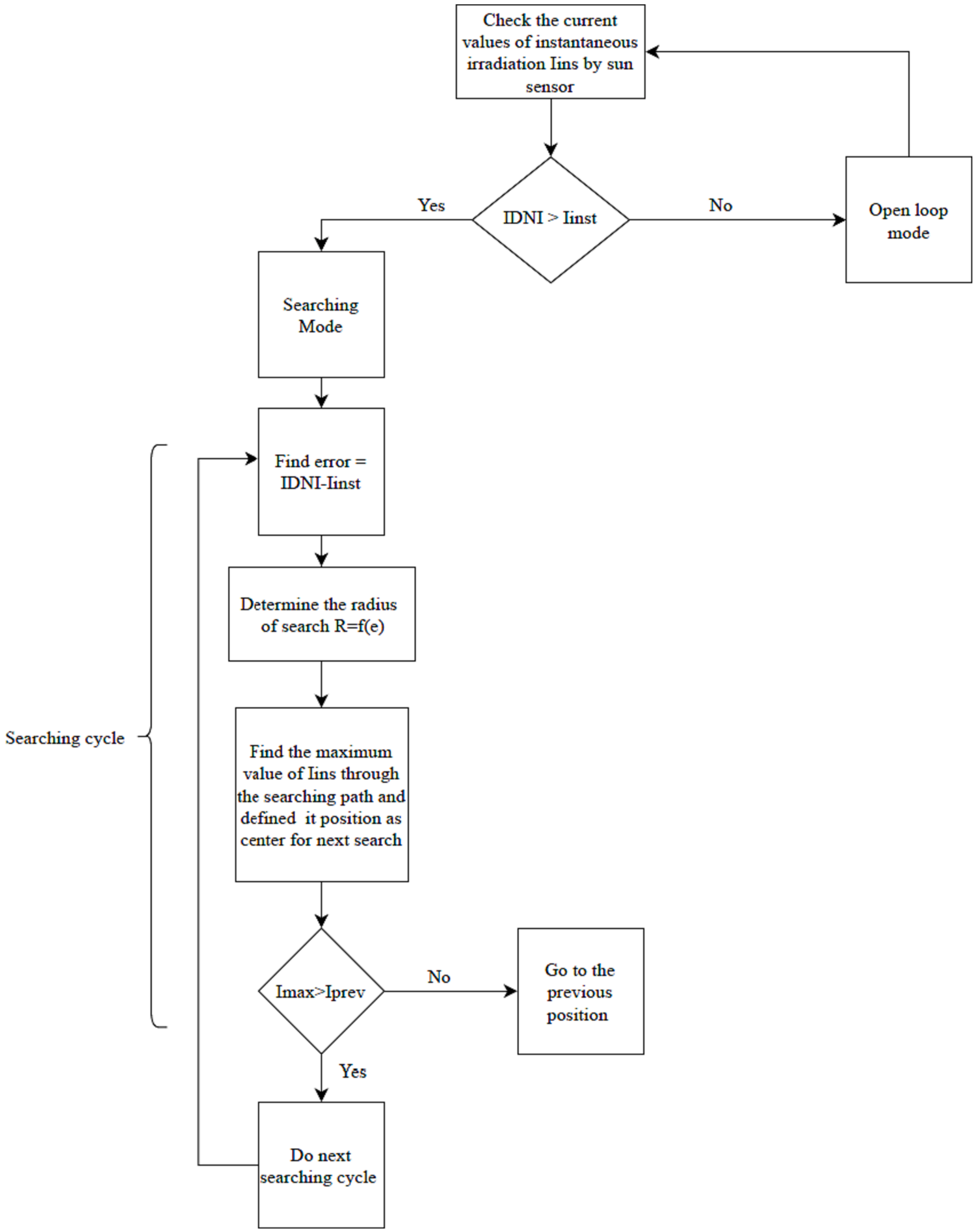

Fig. 12. Flow chart of circular searching mode.

time were kept on an SD card as a lookup table, and a sun angles algorithm was run using MATLAB to track the sun's progress. The stepper motors move the ST intermittently to the new sun position in accordance with the resolution of the encoders, and angles' values are sent based on the time of the real-time clock (RTC).

The module angles are calculated using a MATLAB function and quantized to fulfill the solar tracker minimum angle step before being implemented in the microcontroller (limited by the encoder resolution). Signal quantization is a nonlinear, memory-less, and time-invariant procedure [49]. The microcontroller stores the quantized angles as lookup tables. Due to the microcontroller's reduced execution time, there will be no time lost during the calculation.

The module angles are quantized with a 0.3 step size and a 4-minute sampling duration in Fig. 8. The angles were created for the year's day number 245 (2/9/2021).

The azimuth angle with the Earth's magnetic north and the horizontal angle with the horizon line must be adjusted to zeros because the solar tracker is mobile. This homing procedure is carried out during the

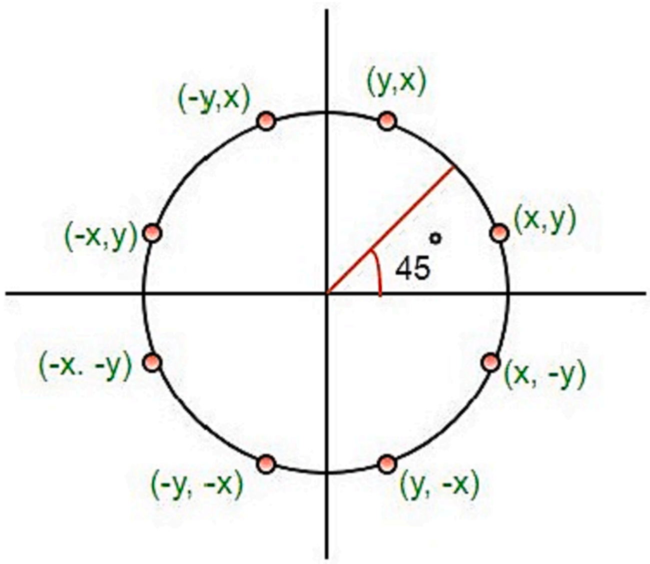

Fig. 13. Eight octans of circle.

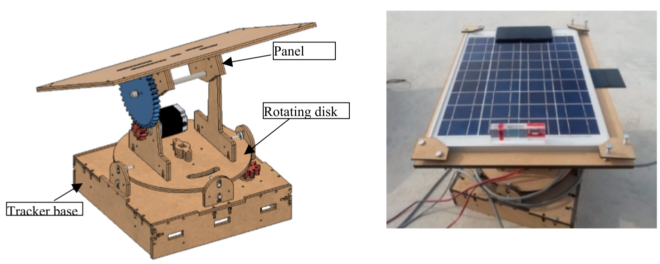

Fig. 14. (a) Mechanical structure of the solar tracker. (b) Homing calibration of solar tracker.

initial run of the microcontroller and is not carried out while the open-loop control system is operating.

The open-loop control system will be used after homing by the program. Every 1 sec, the open-loop control system is interrupted in order to measure the power. The flow diagram for the DAST open-loop control system is shown in Fig. 9. Since the trigonometric equations of the sun's location must be solved in advance, the MATLAB code will calculate the zenith and azimuth angles beforehand and record the results as a lookup table. Each table will have 120 data for angles because the sample period is 4 min (since the starting time is at 8:30 and the end time at 16:30). Each lookup table would be 120 × 4bytes = 480 Bytes, or 0.46875 KB, in size if it contained the value of the angles and their related angles. By storing the angle values and using the database's index as a measure of time, the size of the lookup table can be cut in half. The formula for calculating the index from the time is as follows:

$$index = ax + b$$

$$a = \frac{Number\ of\ values}{T_{end} - T_{start}}$$

$$b = -T_{start} \times \left(\frac{Number\ of\ values}{T_{end} - T_{start}}\right)\ or\ -T_{start} \times a$$

$$Number\ of\ values = \left(\frac{T_{end} - T_{start}}{4min\tilde{A}\cdot 60}\right) \tag{8}$$

Where x is the local time in hours.

3.2. Closed-loop control system of the solar tracker

The closed-loop controller of the solar tracker system is performed depending on feedback value from the small cell, solar cell 0.6 W (sun sensor) is installed on the ST frame. By comparing instantaneous irradiation I_{inst} and direct normal irradiation (DNI) the control mechanism is determined. DNI irradiation indicates the previous values of irradiation on a clear day of the same month from the previous year, as recorded by the irradiation database (DNI) on the Solcast Data base website [50].

The cloud's capacity interacts negatively with DNI due to attenuate of the received irradiance. In winter and spring seasons, DNI is reduced significantly due to effect of clouds bands is evident on the DNI variability related to clouds effect. This is especially noticeable in the cloud-related DNI fluctuation [51]. The technique for solar angles is implemented in MATLAB and saved as a lookup table containing azimuth angle, zenith angle, time, and geographical location. To follow the movement of the sun, the microcontroller takes angles values bases on the time of RTC, and stepper motors oriented ST intermittently to the new sun position according to the resolution of the encoders.

Fig. 10 shows a block schematic of the control system in which the PV panel's power data is stored during the experiment. When the sun's irradiance falls below the DNI irradiance, the hybrid controller switches to a closed-loop system searching algorithm.

3.2.1. Searching mode

This mode is activated if error values between actual irradiance become less than the previous irradiance value. The previous values are represented by the Solcast irradiance data (DNI) on a clear day in the same month of the previous year. DNI data is directly affected by clouds and serves as an indicator of how clouds affect the system. The comparison is conducted based on the irradiance current of PV cells and solar data (DNI). The movement of the structure follows the circular routes depicted in Fig. 11 (S1, S2, S3, and S4). Method of operation consists of the following steps:

1. The searching mode utilizes circular paths which radius is proportional to the difference between the actual and the prior threshold reading irradiance value; hence, it defines the search path.
2. During the search, the system examines the values of all irradiance points by PV cell current path points and identifies the largest reading position in order to define it as the center of the subsequent search.
3. The path's maximum value is compared to the preceding value. If the result is less than the previous value, the search will return to the previous location; otherwise, the search will continue.
4. In order to conserve energy, the system conducts particular rounds of searches; if it is determined that there is no actual improvement in energy capture (due to heavy cloud cover), the system reverts to open-loop control mode.
5. In this study, sun angle models are used as a reference; after 4 min of completing searching circles and attaining the maximum irradiation value, the ST will move based on sun angle data recorded in SD card.

The proposed circular searching path is depicted in Fig. 11; the radius of the circle is directly proportional to the difference between the instantaneous irradiation measurement and the Solcast DNI value. The searching algorithm is performed by checking the instantaneous irradiation values for the circular path, to find the position of the maximum irradiation I_{max}, which is represented as a center for the next cycle. In the case of the value of I_{max} for the current cycle is less than I_{max} for the previous cycle, the system will return to position of I_{max} of the previous cycle, otherwise will be continue in searching.

In the algorithm, there are two special cases:

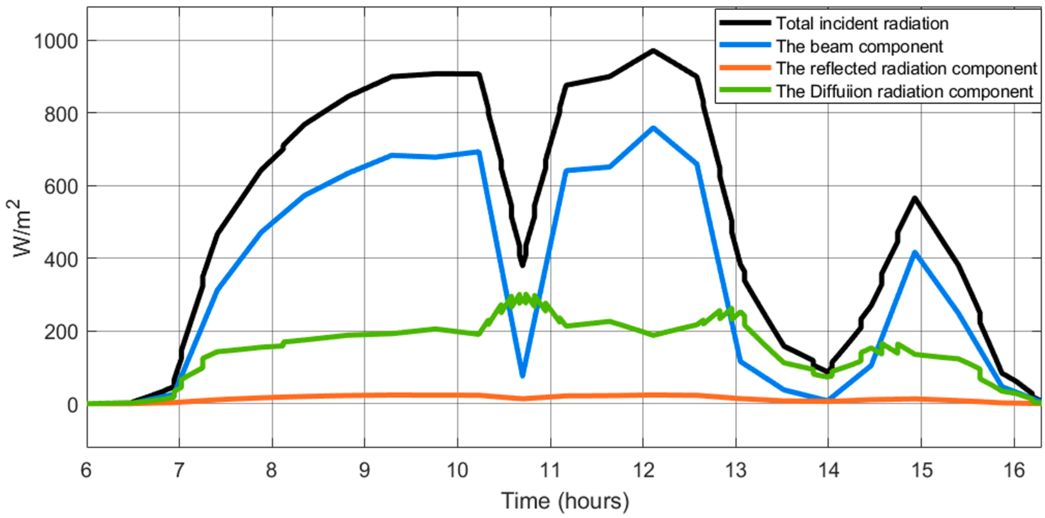

(a)

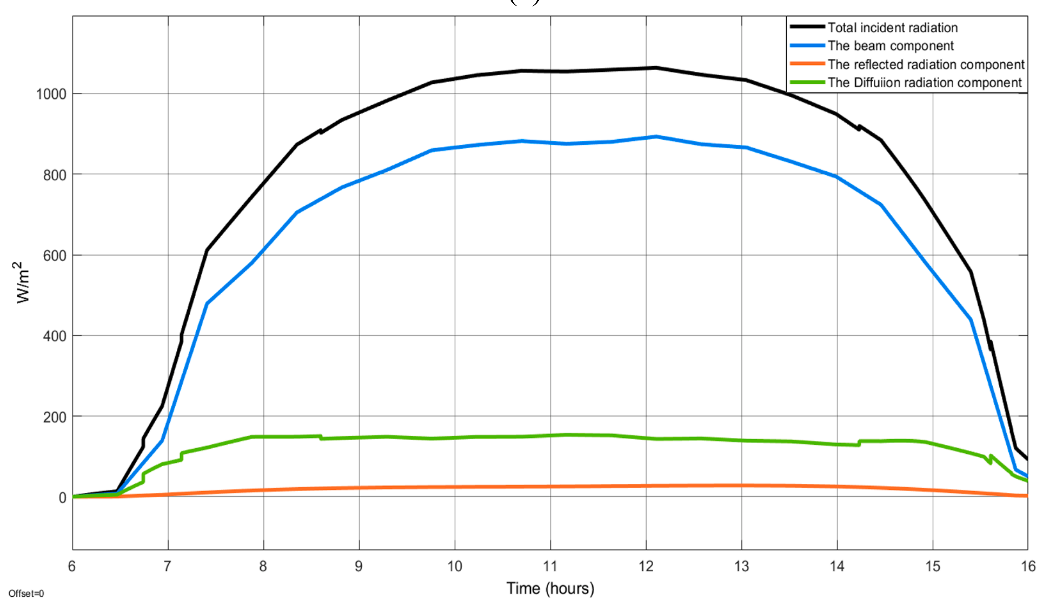

(b)

Fig. 15. (a) Solar irradiation of cloudy day on 19 Nov 2021 (b) ST Solar irradiation of clear day on 23 Nov 2021. The X axis represents the time in minutes.

- The first case is to save energy while searching by limiting the number of searching circles. If there is no advantage from searching owing to heavy clouds and low irradiance value, the system will convert to an open-loop system.
- The second scenario occurs when the search has been completed and the open-loop system's sun angles are utilized as a reference to validate the next step in the ST. Therefore, after four minutes of searching, the ST will be positioned according to the SD card's sun angles (open-loop system).

Fig. 12 is a flowchart illustrating the mechanism of the aforementioned manner of searching. Midpoint circle path drawing is the algorithm used to define the searching path's points.

3.2.2. Midpoint circle path drawing algorithm

The mathematical definition of a circle is a set of points that have the same distance r from the circle's center (X_c, Y_c). The midpoint circle path drawing algorithm is considered as one of the most effective algorithms used for circle drawing [52–54]. The midpoint circle route drawing approach deals with the circle's boundaries as steps, with a step size of 0.3° for the circle's points (encoder resolution). The point location around the circle boundary is determined using Eq. (9):

$$f(x,y) = (x - x_c)^2 + (y - y_c)^2 - r^2 \quad (9)$$

The location of the point based on $f(x,y)$ value:

$$\begin{cases} f(x,y) = 0, \text{ the point is on the circle} \\ f(x,y) < 0, \text{ the point is inside the circle} \\ f(x,y) > 0, \text{ the point is outside the circle} \end{cases} \quad (10)$$

The coordinates of the point at the k^{th} step are located in the midpoint between two steps' boundaries. X and Y coordinates will be incremented or decremented by step size based on the decision parameter P_K. The value of the X coordinate is incremented by unit step in all cases for the first octan, while the value of the Y coordinate is not changed if $P_K < 0$, Otherwise, the value of Y is decremented by the unit step. The circle is divided into 8 octans as shown in Fig. 13.

The procedure for finding the coordinates of the points for the first octan is demonstrated by the steps below:

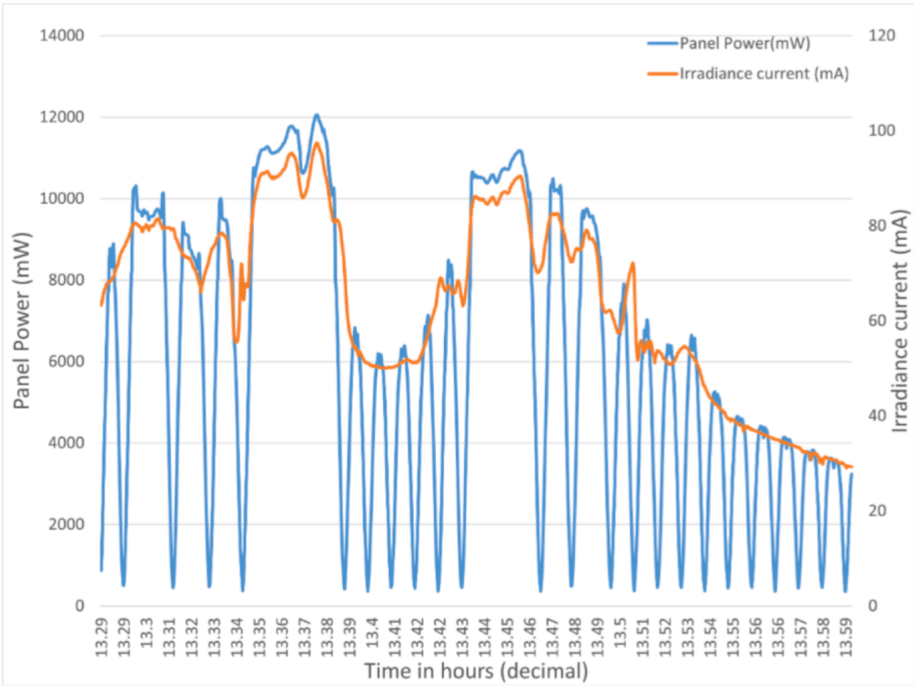

(a)

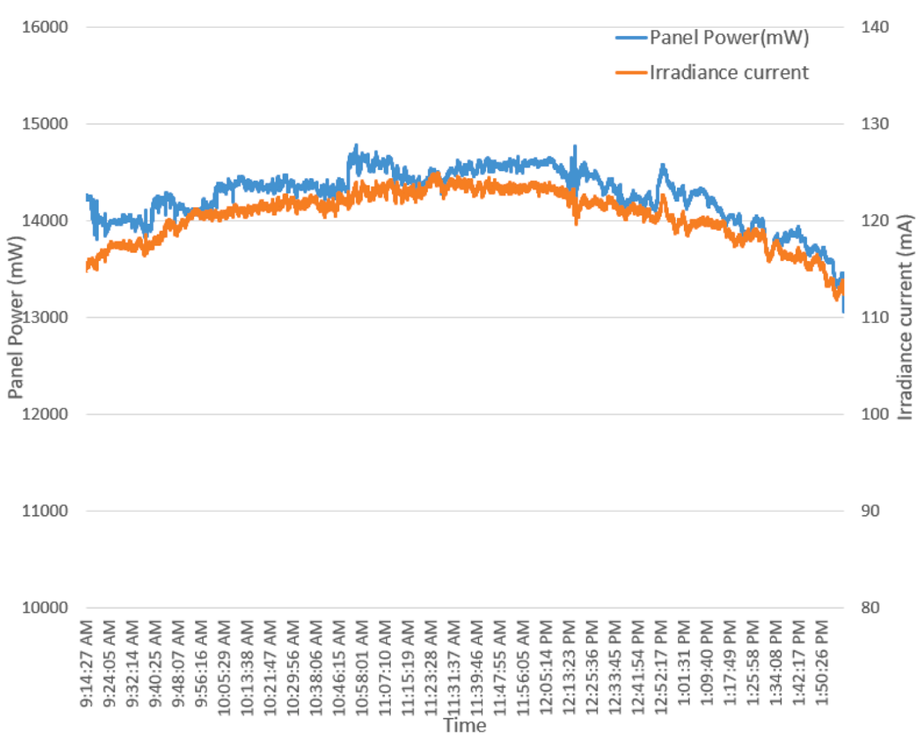

(b)

Fig. 16. a) Irradiance current and panel power on 19 Nov 2021 from 13:29 to 13:59, the blue graph represents the panel power (mW), and the orange graph represents the irradiance sensor current (mA). (b) Irradiance current and panel power on 23 Nov 2021 from 9:14 to 13:54, the blue graph represents the panel power (mW), and the orange graph represents the irradiance sensor current (mA). (For interpretation of the references to colour in this figure legend, the reader is referred to the web version of this article.)

First: Define circle center (X_c, Y_c) and the radius r and define the first point in the octan whose distance from the center is:

$$(X_o, Y_o) = (0, r) \tag{11}$$

Second: Determine the value of the initial decision parameter as:

$$P_0 = \frac{5}{4} - r \tag{12}$$

Third: IF $P_K < 0$, the next point is $(X_k + 1, y_k)$ and next decision parameter will be:

$$P_{K+1} = P_K + 2x_{k+1} + 1 \tag{13}$$

Otherwise, IF $P_K \geq 0$, the next point is $(X_k + 1, y_k - 1)$ and next decision parameter:

$$P_{K+1} = P_K + 2(x_{k+1} - y_{k+1}) + 1 \tag{14}$$

Fourth: calculating the points positions until $x \geq y$, and move the points values as the center position (X_c, Y_c) where:

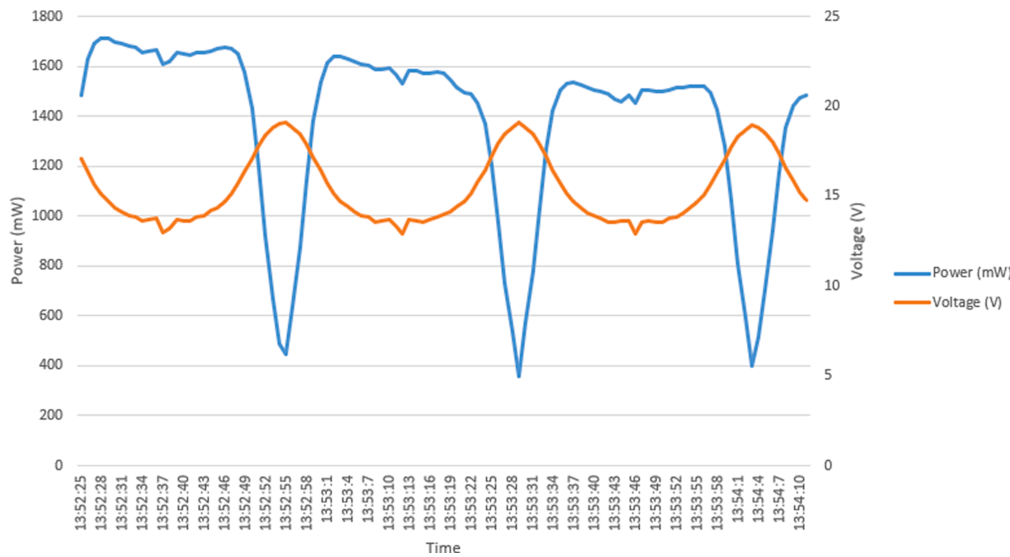

Fig. 17. Power and voltage behavior in heavy cloud conditions (1)13:52:25 to 13:54:10.

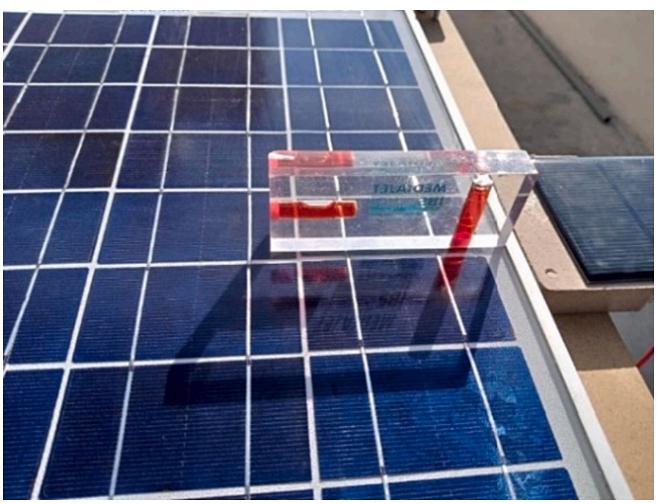

Fig. 18. Positioning the PV cell in parallel with the horizontal surface, the small cell is in the right of the image.

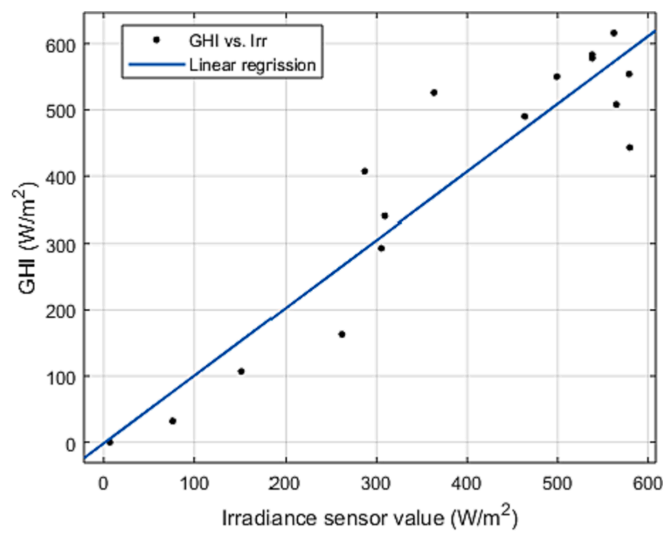

Fig. 19. Linear regression between Irradiance sensor calibration and GHI irradiation values for 24 Nov 2021.

$$x = x + X_c$$
$$y = y + Y_c \tag{15}$$

After finishing the first octan's points, the rest octans points will be found as shown in Fig. 13, (i.e., by flip the x and y coordinate for first octan to find the point of second octan).

3.2.3. Determination of searching radius

According to the mechanical motion range, the ST zenith angle range in the searching mode is approximately 70°. The minimum possible zenith depends on the latitude of the experiment location, and can be found as follows:

$$Min_{zenith} = latitude - Max.declination = 32^{\circ} - 23.45^{\circ} = 8.55^{\circ} \tag{16}$$

Min_{zenith} represents the minimum zenith angle of the sun during the year.

The maximum radius searching path is set to 20°, and the minimum radius angle is defined as 0.9°, where the minimum readable angle of ST is 0.3°.

The Error Ratio (*ER*) represents the ratio between Irradiance sensor and *DNI* irradiance as following:

$$ER = \frac{Irradiance\ sensor}{DNI\ irradiance\ value} \times 100\% \tag{17}$$

Where: *ER* is the error ratio, *Irradiance sensor* is the Instantaneous value of the sensor (W/m^2), and *DNI Irradiance value* is the direct normal Irradiance for a clear day of the experiment month.

The activation of searching mode depends on ER value as follow:

- If ER is less than 1, the ST will continue to operate in open-loop mode; however,
- If ER is greater than 1, the ST will enter searching mode.

ST determines minimum radius value when the *ER* value is in between (0.95–1), where maximum radius is determined when the *ER* is between (0–0.25):

$$MaxRad = Slope \times 0.25 + b$$
$$MinRad = Slope \times 0.95 + b \tag{18}$$

Therefore, slope is found as:

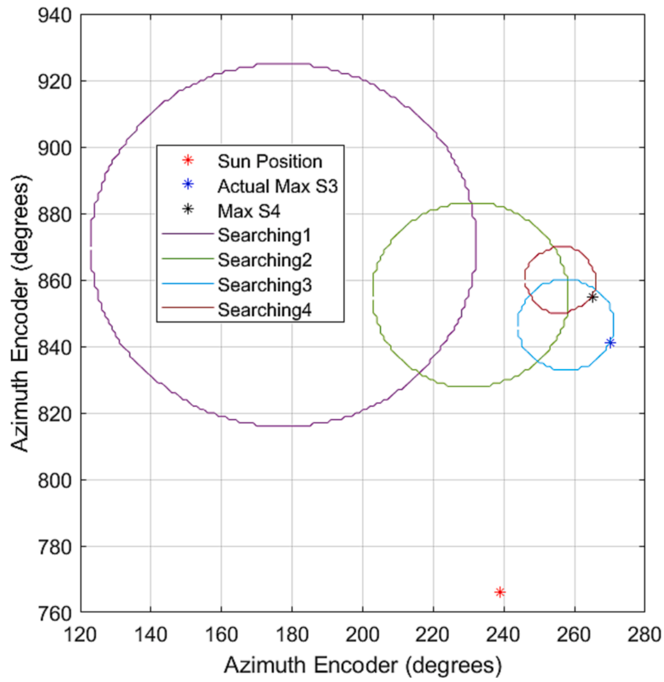

Fig. 20. Searching pattern of ST with displacement −20° (66 pulses) and +30° (100 pulses) for Zenith and azimuth respectively (1pulse = 0.3°).

$$Slope = \frac{MinRad - MaxRad}{0.95 - 0.25}$$
$$b = maxRad - 0.25*Slope \tag{19}$$

4. Results and discussion

The portable solar tracker ST used in this experiment was tested and operated using the mechanical construction depicted in Fig. 14, and the homing position was set up before the experiment. Using a spirit level, the PV panel's initial position was manually adjusted to be parallel to the horizon; the vertical axis was then initialized by rotating the disk to align with the earth's magnetic north.

To align the PV panel with the movement of the sun, the mechanical platform and hybrid control system of flat PV panel should be able to control the physical movement of ST to direct PV panel to sun position. After homing, by using SPA as an open loop system the microcontroller controls the ST using a lookup table that contains estimated sun angles generated by MATLAB. When the solar radiation is less than the DNI radiation, closed-loop system based on a searching algorithm is used by the hybrid controller. The sun's irradiation was measured and sensed using a small PV cell; the cell must first be calibrated before being utilized to sense the sun's irradiation.

For stepper motors, the PID controller is utilized to address two problems:

- Step losses; in the industrial applications stepper motors are used close to the operation boundaries, which make occurs the step losses highly possible the continuous risk of step losing due to overload is one of drawback open-loop position control [55].

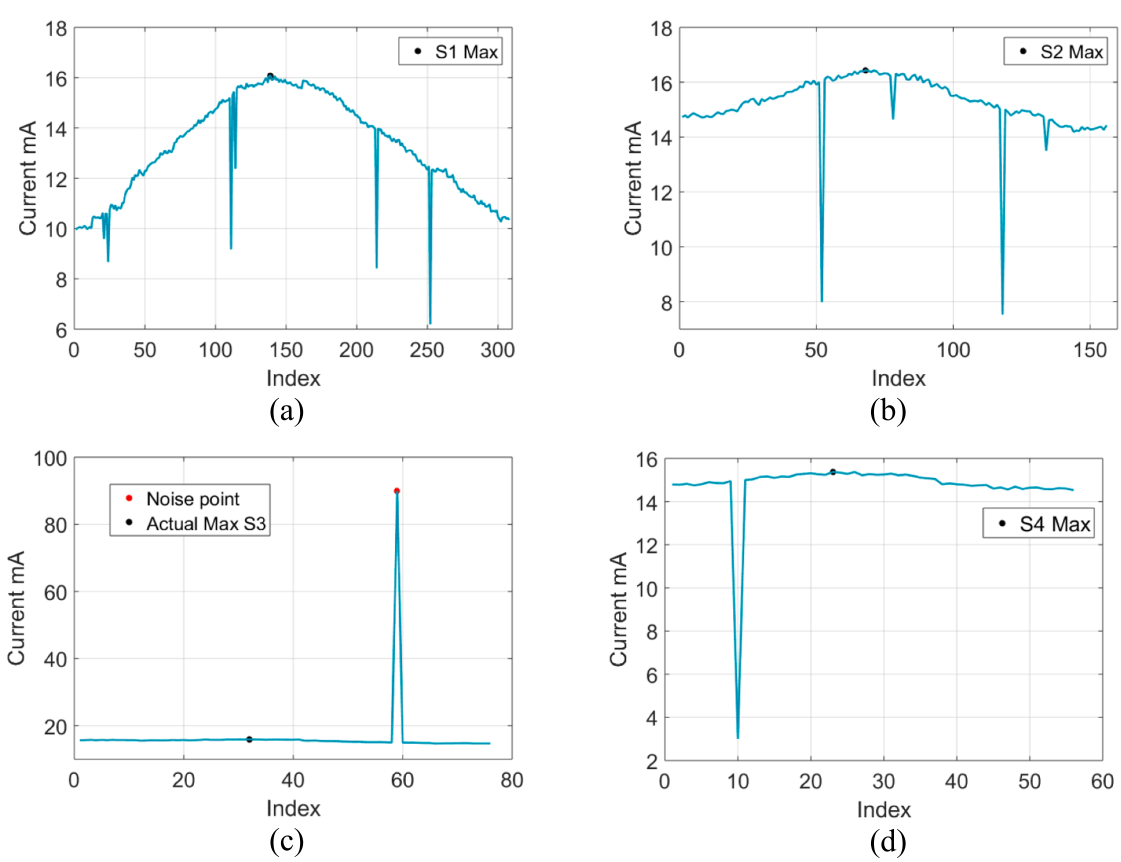

Fig. 21. The Irradiance sensor current values during the searching paths (S1,S2,S3,S4) showing the maximum values during research displacement (−20°, +30°) for ST zenith and azimuth.

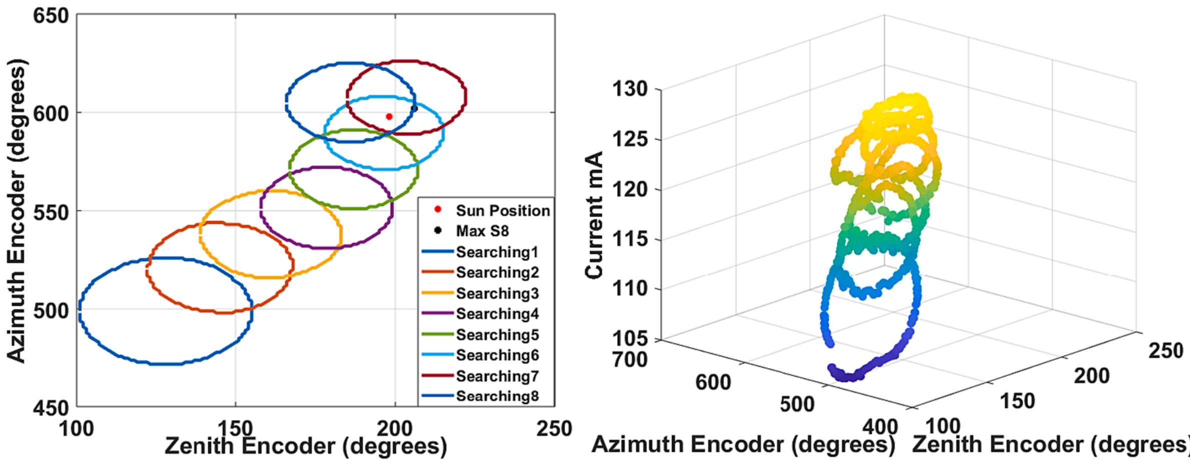

Fig. 22. Searching pattern of ST with a displacement of −21.3° (71 pulses) and −29.7° (99 pulses) for the Zenith and azimuth angles respectively (1pulse = 0.3°) and the induced current.

- Backlash of gears; which is caused by the varying angles between the input shaft and the output shaft and is a result of tooth profile inaccuracy.

After modifying the controller's parameters, we eventually achieve the desired response. The controller's settings were $k_p = 5.6444$, $k_i = 0.4704$, $k_d = 0.5315$.

4.1. Data collection

The ST system records the real-time data of the experiment [Time, Panel voltage (V), Panel current (mA), Panel Power (mW), Irradiance current (mA)]. A sample of the experimental findings will be shown to support the method used. The value of the horizontal irradiation is shown by Solcast weather data every half hour. Based on a sample of Solcast weather data, Fig. 15a depicts the solar radiation of a cloudy day between 6- 17 (19 Nov 2021). Fig. 15b, which depicts the ST's daytime solar irradiation on November 23, 2021, with clear skies.

As depicted in Fig. 16a, the sky had a cloudy appearance. The results indicate that the output power fluctuates depending on the presence of clouds. At 13:37, the recorded power was 11.936 W. The power then declines as the volume of the cloud increases, reaching 1.087 W. In Fig. 16a, it is evident that the sensor current is proportional to the rise in sun irradiation. The short circuit current of the small PV cell is dependent on the irradiance and becomes more stable as the irradiance varies. This can be observed at 13:37, when the short circuit current increases with an increase in ST power (incident radiation) and then declines at 13:52. until the conclusion of the experiment.

In the case of a cloudless sky, the output power behavior demonstrates stability in the values;

- The generated power increased to a maximum of 14.702 W at 11:04, and
- The total amount of energy created during the experiment was 62.854Wh.
- In addition, the output of the small cell's short circuit current increased to 124.11 mA as sun irradiation increased at 11:04.
- The output energy of the simulated MATLAB ST was equal to 64.218 Wh.

The PV output energy was reduced to 2.407 Wh on days with heavy clouds due to the quick change in the amount of irradiance, while the output energy for the simulation was 3.718 Wh.

MPPT charger works to extract the maximum available power from PV panel, the variety irradiance impact on MPP. Perturb and Observe (P&O) algorithm, is used by the MPPT charger to calculate the maximum operation point, the principle of this algorithm is measuring the differences of voltage and power for the instantaneous and previous PV output values, to determine the maximum operation point, as shown in Fig. 17, by comparing the voltage and power differences between the current and prior PV output values.

The operation method is based on periodic increasing or decreasing of the PV voltage, the increasing of PV voltage is in two statements: if ΔP & ΔV > 0, ΔP & ΔV < 0, and the decreasing of PV voltage in two statements: if ΔP < 0 & ΔV > 0, ΔP > 0 & ΔV < 0. If increasing PV voltage leads to decrease the power this means the operation point is in the right of MPP and its need to decrease the voltage to shift the operation point to MPP, and if increasing PV voltage leads to increase the power this means the operation point is in the left of MPP, its need to increase the voltage to shift the operation point to MPP. This process leads to continuously oscillates of PV power around the MPP.

4.2. Sensor calibration

In order to check and monitor the irradiance values based on the module's short circuit current I_{sc}, a PV cell 0.6-Wp c-Si PV module was employed. The INA219 chip is attached to the PV module terminals in order to read I_{sc} values. It is possible to convert I_{sc} to irradiance values using the following formula [56]:

$$Gi_{PV} = \frac{Read(I_{sc}) \times Gi_{ref}}{I_{sc\,ref}} \tag{20}$$

Where: Gi_{PV} is the solar irradiance of the PV module (W/m^2), $Read(I_{sc})$ is the read INA219 chip of short-circuit current (126 mA), Gi_{ref} is the reference value of the solar irradiance at (STC) (1000 W/m^2), and I_{scref} is the short-circuit current of the PV module at STC (126 mA). The calibration of the PV module irradiance sensor was achieved by comparing the sensor readings with Solcast *GHI* irradiance values, which have been read every half hour. *GHI* is the total irradiance value for the horizontal surface. The experiment was carried out by reading the data from the read INA219 chip of the short-circuit current cell over the course of a day after making the cell parallel to the horizontal surface as shown in Fig. 18.

The calibration is carried out using linear regression, and the coefficient of determination is calculated as ($R^2 = 0.8649$), which indicates that 86.49% of the points are fitted in the regression line, and the correlation is equal to (R = +0.93). The presence of a positive sign indicates that the readings from the irradiance sensor and GHI are positively correlated. The percentage of correlation between GHI and varying irradiance sensor values is 93%.

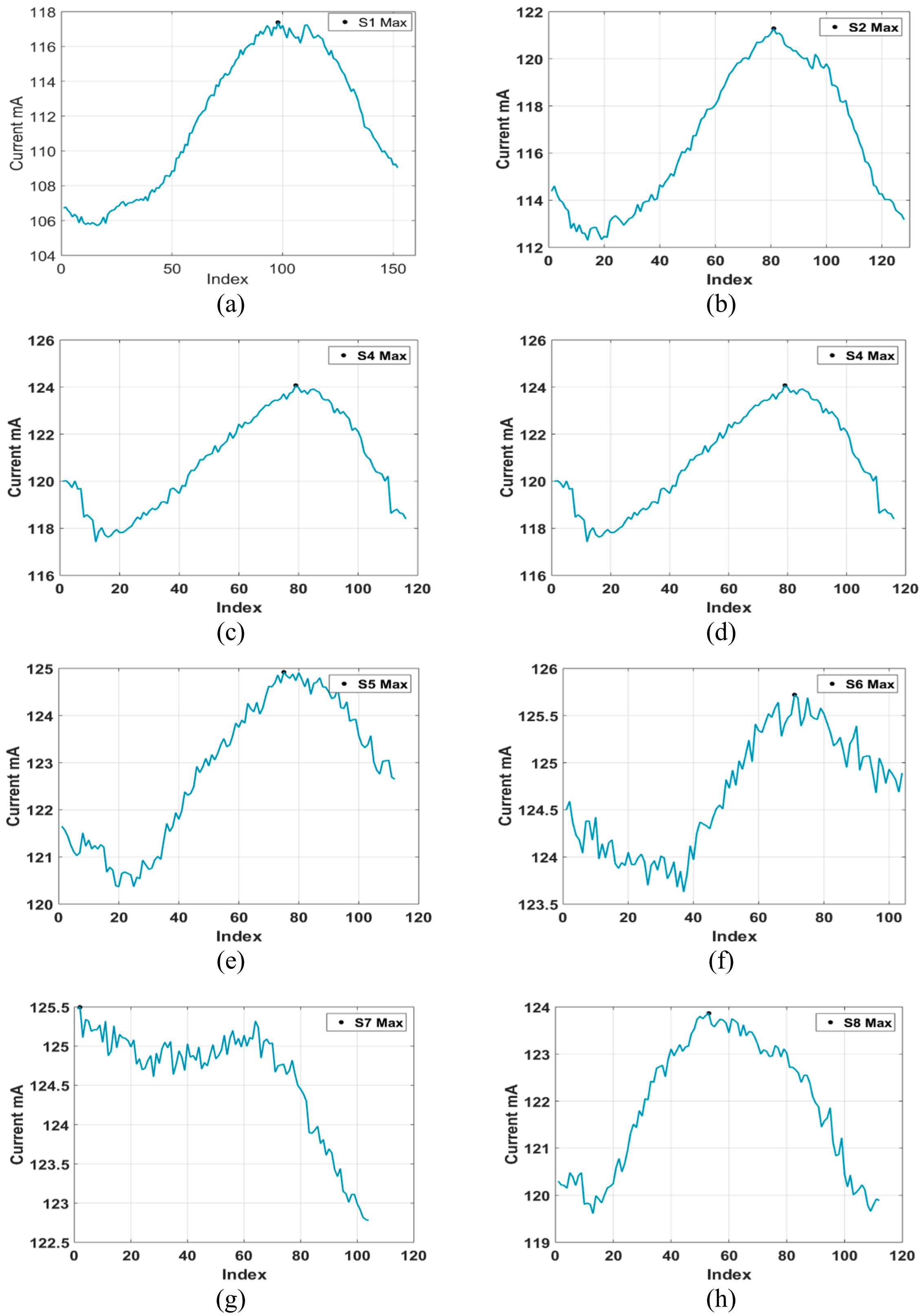

Fig. 23. The Irradiance sensor current values during the searching paths (S1-S8) showing the maximum values during research displacement (−21.3°, −29.7°) for ST zenith and azimuth.

Table 3
Convergence and divergence experiment summary.

Displacement from the sun angles		No. circles	Effect	Percentage error	
Azimuth	Zenith			Azimuth	Zenith
−30°	−20°	4	Positive noises and the radius were (R, R/2, R/4, R/6) where R equals 16.2°	4.83029%	−8.786611%
+30°	−20°	4	Positive noises and the radius were (R, R/2, R/4, R/6) where R equals 16.2°	−11.573%	−9.016%
−31.2°	−30.3°	4	Average filter and the radius were (R, R/2, R/4, R/6) where R equals 16.2°	5.234%	12.857%
−15°	−30°	4	Average filter and the radius were (R, R/2, R/4, R/6) where R equals 16.2°	−1.89%	5.909%
−21.3°	−29.7°	8	Average filter and radius determination based on the proposed algorithm	−0.6689%	−4.0404%

The calibration equation used to correct the error in irradiance sensor reading is given as:

$$Irradiance\ value = 1.0212x - 1.5617 \quad (22)$$

$$Irradiance\ value = 1.0212\left(\frac{Read(I_{sc}) \times Gi_{ref}}{I_{scref}}\right) - 1.5617 \quad (23)$$

Fig. 19 displays the linear regression between Irradiance sensor calibration and GHI irradiation values for the 24th of November 2021 for situations where the irradiance value is the calibrated solar irradiance (W/m^2).

4.3. Convergence and divergence of circular searching path using PV-based irradiance sensor: Clear sky case

The converge and diverge experiment was executed to make sure of the circular searching behavior when using irradiation current as feedback for circular searching, in terms of convergence and divergence of ST from the sun position. This experiment was implemented in the clear sky, for this it's difficult to use DNI irradiance as a factor to determine the searching radius as shown in 3.5.3 Section. The searching paths are restricted to 4 paths and the radius for paths is (R, R/2, R/4, R/6) where R equals 16.2° (54 pulses).

Fig. 20 represents the searching results when the displacement of the ST is −20° (66 pulses) for Zenith angle and +30° (100 pulses) for azimuth angle; the time of the experiment was 15:54:22 on the 25th of November 2021.

Fig. 21 represents the behavior of the irradiance sensor current values during the searching paths, Fig. 21(a,b,d) show values that were affected by negative noise which caused a variation in the paths' directions, while Fig. 21(c) shows the appearance of a positive noise value during the third searching circle, but it was far from the actual point of this path. Therefore, it contributed to the increase in the error rate.

Another experiment was executed on a day with a clear sky by displacing the ST position with −21.3° (71 pulses) for the Zenith angle and −29.7° (99 pulses) for the azimuth angle from the sun's position to monitor the searching behavior. In this experiment, we assumed 160 mA as the Irradiance current for DNI on a clear day to convince ST that it is working in cloudy weather. Fig. 22 represents the shape of searching when displacing the ST, the time of the experiment was 11:22:42 from the 27th of November 2021.

After using the average filter, the behavior of the irradiance sensor current values during the searching paths is shown in Fig. 23. For each circle, the search algorithm chose the highest irradiance current. The irradiance current values increased as the number of search circles increased till it reached the seventh search circle. After reaching the position of the sun, the irradiance current falls in circle 8 because of the fixed radius of circles.

The Azimuth and zenith angles for the sun's location were 179.4° and 59.4°, respectively. The irradiance current and angles' error values had a reverse relationship in which the current increasing during searching circles until it reached the seventh circle, and then reduced in circle 8 as a result of the circle-radius values becoming fixed when it reached the position of the sun. This constancy of radius values (5.4°) back to assume 160 mA represents the solar irradiance on the clear day for convincing ST that it is working in cloudy weather.

The findings were filtered by taking the mean of 100 values for one measurement in order to reduce the random noises during searching circles. The convergence and divergence experiments are summarized in Table3, which also shows how utilizing the mean value affects the searching process.

In the case of a clear sky day, convergence and divergence experiments were conducted to examine the behavior of the seeking direction, specifically if it is going toward or away from the position of the sun. The circular searching method is intended to function on overcast days or when the instantaneous radiation I_{rr} is reduced, and to calculate the searching radius R depending on this reduction. R is therefore established for the initial four tests.

The first and second experiments, as shown in the results, exhibited positive noises, which increased the error rate of azimuth and zenith angles. The fourth experiment reduced the mistakes by filtering the data using the mean values, but the third experiment had two major limitations: the value of the displacement (−31.2°, −30.3°), and the radius of the confined circle. The final experiment uses the circular searching technique, which includes calculating the circle radius using Irr. Circles' radii were within a narrow range of 7.8° to 5.7° of one another, and their error values were lower than in the other experiments.

4.4. Circular searching path algorithm under cloudy weather

The final experiment is executed on a cloudy day on the 3rd of December 2021. Three search operations are conducted during the experiment; Fig. 24 depicts the behavior of the searching circles. In order to demonstrate the impact of employing a hybrid controller that alternates between open-loop and closed-loop controls systems, this experiment was carried out. As the radius decreases, the steps of ST motion become sharper, as shown in Fig. 24. The final circle in (a) has the smallest radius (0.9°). Fig. 24 leads to the conclusion that the position of the sun during foggy weather does not necessarily represent the strongest solar radiation.

The irradiance current values Irr during the searching processes are shown in Fig. 25, which indicated by colors; blue represents less values and yellow represents the higher values in each searching operation. Fig. 25(a,b) demonstrates that compared to the other processes, the effects of clouds were lessened. Due to the influence of the clouds, the last circle in the second and third operations didn't achieve the minimum radius, whereas the final circle does. Fig. 25. The irradiance current values grow during the search circles until they approach the position of the sun, as shown in Fig. 25(a, c, d). The ST was operating in open-loop

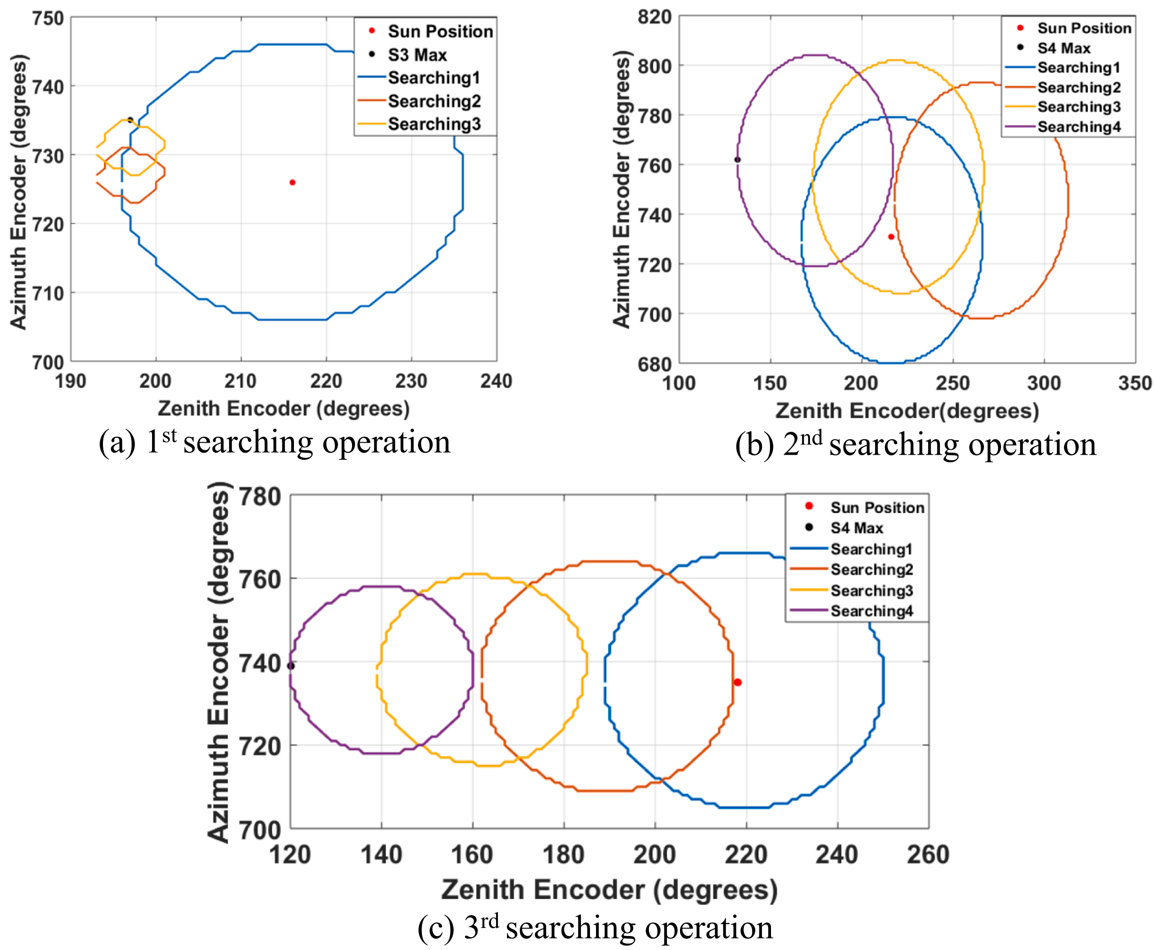

Fig. 24. The behaviour of circular searching path algorithm (1pulse = 0.3°).

mode prior to searching, Table 4 displays the results of applying the searching path algorithm.

As can be seen, the ST will enter searching mode when the irradiance current drops down below the reference irradiance current (determined from the DNI measurements). The path's radius changes depending on the difference between the actual irradiance current and the reference irradiance current. The findings indicated that applying the suggested search strategy led to a 35% increase in generated power.

The search strategy can be implemented using machine learning techniques, which are gaining popularity in solar energy research due to their capacity to optimize solar panel characteristics for maximum energy production. In this aspect, these algorithms can anticipate PV performance under varied weather circumstances and then alter the solar panel's orientation depending on real-time data received. Using past weather data, they can also construct predictive models of PV performance, discovering trends and correlations between weather conditions and PV performance. In addition, they can alter the solar panel's orientation in real time based on the expected performance of the PV cells. Thus, machine learning predictions of PV performance and sun tracker control can significantly improve the efficiency and cost-effectiveness of solar energy production, thereby facilitating the transition to a sustainable and renewable energy future [57–60].

As future works, the proposed system will present as guild devices in solar trackers farm during cloudy weather, by covering a specific area of large PV trackers to save energy consumption during seeking for the large systems.

5. Conclusion

New search algorithms that control the orientation of the panel are required in order to provide the maximum amount of electricity that PV cells can capture regardless of the weather. The aim of this study was to design a sun-tracking system capable of adjusting the orientation of the solar panel to produce the highest amount of electrical production from solar energy in Jordan, irrespective of the local climate.

- A hybrid controller with an open-loop solar monitoring system and an active search algorithm-based dynamic feedback controller were implemented. Real-time measurements of PV panels' declining sun irradiance form the algorithm.
- If the instantaneous irradiance falls below a threshold (DNA for a clear day in each month), the system uses the recently proposed circular path finding method to locate the Maximum Power Point Tracking (MPPT).
- Positive irradiance current noises increased convergence and divergence errors. However, filtering values reduced noise during searching circles, lowering azimuth and zenith angle error rates and increasing irradiance current values.
- The PV cell 0.6-Wp c-Si PV module irradiance sensor was calibrated by comparing sensor data to half-hour Solcast GHI values. The linear regression calibration had a coefficient of determination of (R^2 = 0.8649), meaning that 86.49% of the points were fitted in the regression line, and a correlation of (R = +0.93), indicating a positive link between GHI and irradiance sensor data.

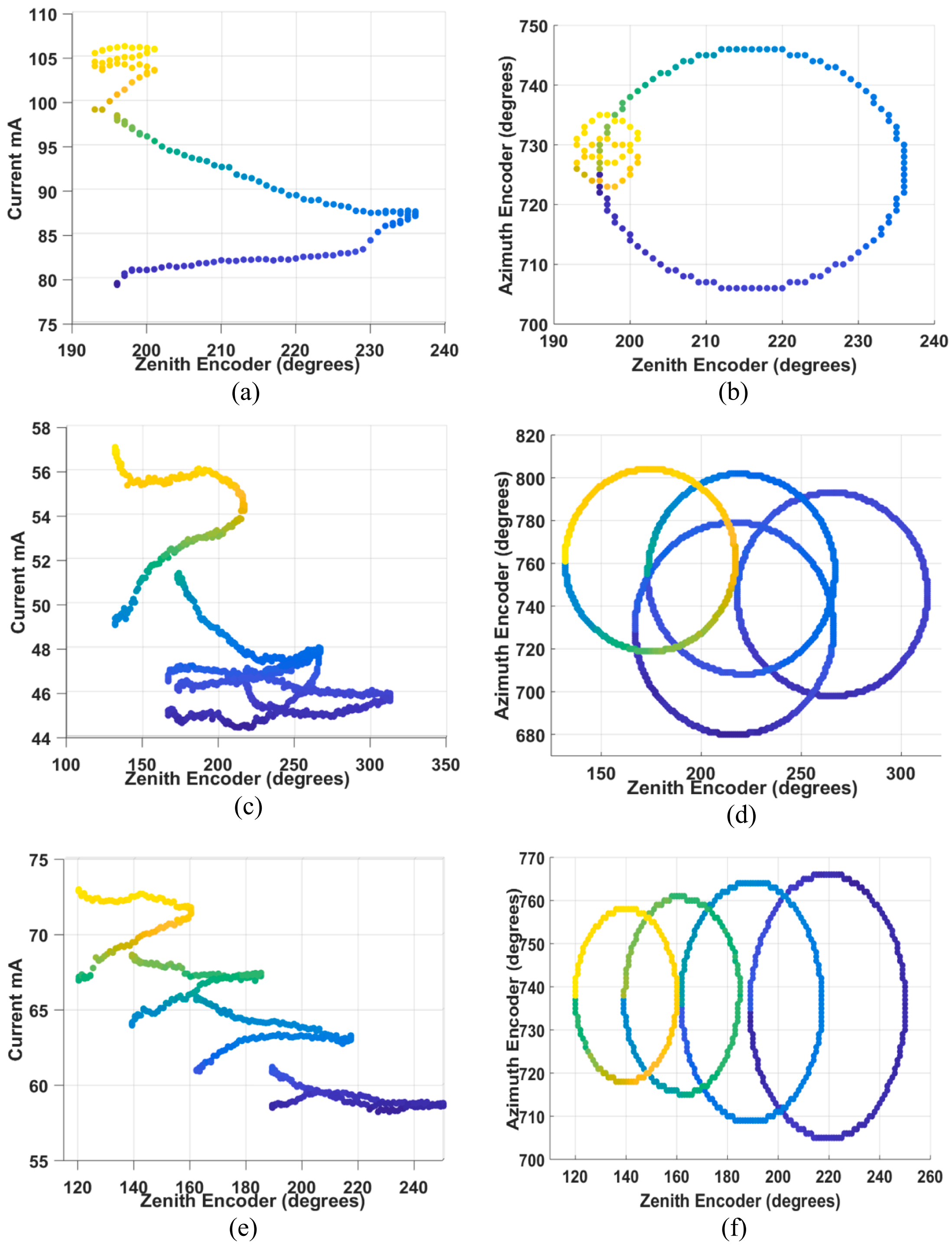

Fig. 25. The Irradiance sensor current values during the searching operations and the searching path behaviour, (a,b) the first search, (c,d) the second search, (e,f) the third search (1pulse = 0.3°).

- On a clear day, the experiment's output power stabilized and increased to 14.702 W. The experiment created 62.854 Wh, where the simulated MATLAB ST output 64.21812 Wh; The experimental results of clear and cloudy day were showed the actual behavior of ST within environment conditions, while the simulated results represent the ST behavior as a theoretical model, this explains the differences between the simulation values and the experiment values.
- Cloudy weather was used to test the sun tracker hybrid control system's circular searching path algorithm. The first, second, and third search operations took 36 s, 2 min, 59 s, and 23 s, respectively, depending on the circle radius. The suggested search method increased generated power by 37.67%, 35.98%, and 30.92% for the 1st, 2nd, and 3rd search operations, respectively, compared to open-loop system. Due to diffuse radiation, the sun angles model in cloudy conditions does not represent the optimal orientation.

Declaration of Competing Interest

The authors declare that they have no known competing financial interests or personal relationships that could have appeared to influence

Table 4
The results of using the circular searching path algorithm in cloudy weather.

Searching Operation	1st	2nd	3rd
Starting time	13:55:03	14:02:15	14:08:58
Irr_{ref}(mA)	100	100	89
R (1pulse = 0.3°)	19 (5.7°)	49 (14.7°)	30 (9°)
Irr (mA)	77.26	44.29	57.85
Power before (mW)	8605.09	4642.35	6289.74
Finishing time	13:55:39	14:05:14	14:11:21
R (1pulse = 0.3°)	3 (0.9°)	42 (12.6°)	19 (5.7°)
Irr (mA)	106.19	57.08	72.93
Power after (mW)	11846.75	6312.95	8234.33
Enhancement in the generated power (%)	37.67	35.98	30.92

the work reported in this paper.

References

[1] Piotr Bojek. (2022, September). *Renewables*. Energy system overview, License CC By 4.0, from https://www.iea.org/reports/renewables.
[2] Jäger-Waldau, A., 2022. Snapshot of photovoltaics–February 2022. EPJ Photovolt. 13, 9. https://doi.org/10.1051/epjpv/2022010.
[3] Haegel, N.M., Verlinden, P., Victoria, M., Altermatt, P., Atwater, H., Barnes, T., Bett, A.W., 2023. Photovoltaics at multi-terawatt scale: waiting is not an option. Science 380 (6640), 39–42.
[4] Ministry of Energy and Mineral Resources (MEMR). (2017). Annual Reports. Retrieved from https://www.memr.gov.jo/En/NewsDetails/Annual_Report_2017.
[5] Abu-Rumman, G., Khdair, A.I., Khdair, S.I., 2020. Current status and future investment potential in renewable energy in Jordan: An overview. Heliyon 6 (2), e03346.
[6] Awasthi, A., Shukla, A.K., S.r., M.M., Dondariya, C., Shukla, K.N., Porwal, D., Richhariya, G., 2020. Review on Sun Tracking Technology in solar PV system. Energy Rep. 6, 392–405.
[7] Wibowo, H., Bow, Y., Sitompul, C.R., 2021. Performance comparison analysis of fixed and solar-tracker installed panel at PV System. IOP Conf. Ser.: Earth Environ. Sci. 709 (1), 012003 https://doi.org/10.1088/1755-1315/709/1/012003.
[8] Y. L. Chua, Y. K. Yong, Y. Y. Koh, (2017, September). Performance comparison of single axis tracking and 40° solar panels for sunny weather, in: *AIP Conference Proceedings* (Vol. 1885, No. 1, p. 020082). AIP Publishing LLC. https://doi.org/10.1063/1.5002276.
[9] Sun, S.-S., Brooks, J., Nguyen, T., Harding, A., Wang, D., David, T., 2014. Novel organic and polymeric materials for solar energy conversions. Energy Procedia 57, 79–88. https://doi.org/10.1016/j.egypro.2014.10.011.
[10] Rezk, H., Aly, M., Al-Dhaifallah, M., Shoyama, M., 2019. Design and hardware implementation of new Adaptive Fuzzy Logic-based MPPT control method for photovoltaic applications. IEEE Access 7, 106427. https://doi.org/10.1109/access.2019.2932694.
[11] Kang, H., Hong, T., Lee, M., 2019. Technical performance analysis of the smart solar photovoltaic blinds based on the solar tracking methods considering the climate factors. Energy Build. 190, 34–48. https://doi.org/10.1016/j.enbuild.2019.02.013.
[12] Alici, H., Esenboga, B., Oktem, I., Demirdelen, T., Tumay, M., 2021. Designing and performance analysis of solar tracker system: A case study of Çukurova region. Design Anal. Appl. Renew. Energy Syst. 165–184 https://doi.org/10.1016/b978-0-12-824555-2.00004-6.
[13] Shafie, S., Kadir, M.Z., Azis, N., Radzi, M.A., Zuha, W.H., Mustafa, M.A., 2018. High efficiency portable solar generator utilizing optimum solar panel orientation. In: 2018 IEEE 5th International Conference on Smart Instrumentation, Measurement and Application (ICSIMA). https://doi.org/10.1109/icsima.2018.8688811.
[14] Myers, D.R., 2012. Solar radiation resource assessment for renewable energy conversion. Compr. Renew. Energy 213–237. https://doi.org/10.1016/b978-0-08-087872-0.00112-8.
[15] Rubio, F.R., Ortega, M.G., Gordillo, F., López-Martínez, M., 2007. Application of new control strategy for Sun Tracking. Energ. Conver. Manage. 48 (7), 2174–2184. https://doi.org/10.1016/j.enconman.2006.12.020.
[16] Seme, S., Štumberger, G., 2011. A novel prediction algorithm for solar angles using solar radiation and differential evolution for dual-axis sun tracking purposes. Sol. Energy 85 (11), 2757–2770. https://doi.org/10.1016/j.solener.2011.08.031.
[17] Yao, Y., Hu, Y., Gao, S., Yang, G., Du, J., 2014. A multipurpose dual-axis solar tracker with two tracking strategies. Renew. Energy 72, 88–98. https://doi.org/10.1016/j.renene.2014.07.002.
[18] Ikhwan, M., Mardlijah, Imron, C., 2018. Model predictive control on dual axis solar tracker using MATLAB/Simulink Simulation. In: 2018 International Conference on Information and Communications Technology (ICOIACT). https://doi.org/10.1109/icoiact.2018.8350791.
[19] Mitrofanov, S.V., Baykasenov, D.K., Suleev, M.A., 2018. Simulation model of autonomous solar power plant with dual-axis solar tracker. In: 2018 International Ural Conference on Green Energy (UralCon). https://doi.org/10.1109/uralcon.2018.8544275.
[20] Fathabadi, H., 2016. Novel high efficient offline sensorless dual-axis solar tracker for using in photovoltaic systems and solar concentrators. Renew. Energy 95, 485–494.
[21] Toylan, H., 2017. Performance of dual axis solar tracking system using fuzzy logic control: a case study in Pinarhisar, Turkey. Eur. J. Eng. Nat. Sci. 2 (1), 130–136.
[22] Mamlook, R., Ahamed, I., Maqbool, S.D., Al-Ammar, E.A., 2016. A fuzzy simulated annealing algorithm for minimizing consumer electricity bill under demand response. Int. J. Comput. Sci. Inf. Secur. (IJCSIS) 14, 144–160.
[23] Sidek, M.H.M., Hasan, W.Z.W., Kadir, M.Z.A.A., Shafie, S., Radzi, M.A.M., Ahmad, S.A., Marhaban, M.H., 2014. GPS based portable dual-axis solar tracking system using astronomical equation. In: 2014 IEEE International Conference on Power and Energy (PECon). https://doi.org/10.1109/pecon.2014.7062450.
[24] Alia, M.A., Younes, T.M., Subah, S.A., 2011. A design of a PID self-tuning controller using labview. J. Softw. Eng. Appl. 04 (03), 161–171. https://doi.org/10.4236/jsea.2011.43018.
[25] Jamroen, C., Komkum, P., Kohsri, S., Himananto, W., Panupintu, S., Unkat, S., 2020. A low-cost dual-axis solar tracking system based on digital logic design: Design and implementation. Sustainable Energy Technol. Assess. 37, 100618.
[26] Saldivar-Aguilera, T.Q., Valentín-Coronado, L.M., Peña-Cruz, M.I., Diaz-Ponce, A., Dena-Aguilar, J.A., 2023. Novel closed-loop dual control algorithm for solar trackers of parabolic trough collector systems. Sol. Energy 259, 381–390.
[27] Abu-Khader, M.M., Badran, O.O., Abdallah, S., 2008. Evaluating multi-axes sun-tracking system at different modes of operation in Jordan. Renew. Sustain. Energy Rev. 12 (3), 864–873. https://doi.org/10.1016/j.rser.2006.10.005.
[28] Fuentes-Morales, R.F., Diaz-Ponce, A., Peña-Cruz, M.I., Rodrigo, P.M., Valentín-Coronado, L.M., Martell-Chavez, F., Pineda-Arellano, C.A., 2020. Control algorithms applied to active solar tracking systems: A review. Sol. Energy 212, 203–219.
[29] Saymbetov, A., Mekhilef, S., Kuttybay, N., Nurgaliyev, M., Tukymbekov, D., Meiirkhanov, A., Dosymbetova, G., Svanbayev, Y., 2021. Dual-axis schedule tracker with an adaptive algorithm for a strong scattering of sunbeam. Sol. Energy 224, 285–297.
[30] Y. Ahuja, G. Singh, S.M. Singh, S. Bhat, S.K. Saha, Development and deployment of a hybrid controller for a dual-axis solar tracker system, in: 2022 International Conference on Electrical, Computer, Communications and Mechatronics Engineering (ICECCME) (pp. 1-6). IEEE.
[31] Safan, Y.M., Shaaban, S., Abu El-Sebah, M.I., 2018. Performance evaluation of a multi-degree of freedom hybrid controlled dual axis solar tracking system. Sol. Energy 170, 576–585. https://doi.org/10.1016/j.solener.2018.06.011.
[32] I. Reda, A. Andreas, *Solar position algorithm for solar radiation applications (revised)* (No. NREL/TP-560-34302). National Renewable Energy Lab.(NREL), Golden, CO (United States) (2008).
[33] M. Elgeziry, T. Hatem, Designing a dual-axis Open-loop solar tracker for CPV applications, in: *2020 47th IEEE Photovoltaic Specialists Conference (PVSC)* (pp. 1522-1524). IEEE (2020).
[34] R. Rinaldi, B.S. Aprillia, C. Ekaputri, M. Reza, Design of open loop single axis solar tracker system, in: *IOP Conference Series: Materials Science and Engineering* (Vol. 982, No. 1, p. 012016). IOP Publishing.
[35] Saeedi, M., Effatnejad, R., 2021. A new design of dual-axis solar tracking system with LDR sensors by using the wheatstone bridge circuit. IEEE Sens. J. 21 (13), 14915–14922.
[36] A. Suryanto, N. Hudallah, T. Andrasto, C.F. Adhiningtyas, S.A. Khusniasari, Dual-axis solar tracking system based on Raspberry Pi imaging, in: *IOP Conference Series: Earth and Environmental Science* (Vol. 700, No. 1, p. 012016). IOP Publishing.
[37] Ahmed, R., Oh, S.J., Mehmood, M.U., Kim, Y., Jeon, G., Han, H.J., Lim, S.H., 2021. Computer vision and photosensor based hybrid control strategy for a two-axis solar tracker-Daylighting application. Sol. Energy 224, 175–183.
[38] M.H.S. Hameed, M.Z. Hasan, J.A.M. Jobran, Design on real time control for dual axis solar tracker for mobile robot, in: *Proceedings of the 11th National Technical Seminar on Unmanned System Technology 2019* (pp. 1155-1172). Springer, Singapore, (2021).
[39] D. Rahmawati, W. Priharti, M.I.Y. Mardiana, A prototype of solar panel position control system based on image processing. In *IOP Conference Series: Materials Science and Engineering* (Vol. 830, No. 3, p. 032045). IOP Publishing. (2020, April).
[40] J. Zhao, W. Liu, R. Xia, H. Bian, Research on algorithm of optimized sub-regional scanning path generation for RPM, in: 2007 International Conference on Mechatronics and Automation, Harbin, China, 2007, pp. 587-592, doi: 10.1109/ICMA.2007.4303609.
[41] Chen, X., Li, J., Sui, Y., 2020. A new stitching method for dark-field surface defects inspection based on simplified target-tracking and path correction. Sensors 20, 448. https://doi.org/10.3390/s20020448.
[42] Kargar-Barzi, A., Mahani, A., 2020. H-V scan and diagonal trajectory: accurate and low power localization algorithms in WSNs. J. Ambient Intell. Hum. Comput. 11 (7), 2871–2882.
[43] Loutzenhiser, P.G., Manz, H., Felsmann, C., Strachan, P.A., Frank, T., Maxwell, G. M., 2007. Empirical validation of models to compute solar irradiance on inclined surfaces for building energy simulation. Sol. Energy 81 (2), 254–267.
[44] Solcast API. Solar Irradiance Data. Retrieved from https://solcast.com.
[45] Ajdid, R., Ouassaid, M., Maaroufi, M., 2017. Modeling and simulation of a novel photovoltaic solar system. Int. J. Energy Convers. (IRECON) 5 (6), 171–179. https://doi.org/10.15866/irecon.v5i6.13802.
[46] Gevorkian, P., 2008. Solar Power in Building Design: The Engineer's Complete Design Resource. McGraw-Hill, New York, NY.
[47] Duffie, J.A., Beckman, W.A., 2020. Solar Engineering of Thermal Processes. Wiley, Hoboken, NJ.

[48] Elbreki, A.M., Alghoul, M.A., Al-Shamani, A.N., Ammar, A.A., Yegani, B., Aboghrara, A.M., Rusaln, M.H., Sopian, K., 2016. The role of climatic-design-operational parameters on combined PV/T collector performance: A critical review. Renew. Sustain. Energy Rev. 57, 602–647.

[49] Santina, M.S., Stubberud, A.R., 2005. Basics of sampling and quantization. In: Hristu-Varsakelis, D., Levine, W.S. (Eds.), Handbook of Networked and Embedded Control Systems. Birkhäuser, Boston, MA, pp. 45–69.

[50] Bright, J.M., 2019. Solcast: Validation of a satellite-derived solar irradiance dataset. Sol. Energy 189, 435–449.

[51] Prasad, A.A., Taylor, R.A., Kay, M., 2015. Assessment of direct normal irradiance and cloud connections using satellite data over Australia. Appl. Energy 143, 301–311.

[52] M. Cao, S. Liu, F. Cao, Midpoint distance circle generation algorithm based on midpoint circle algorithm and Bresenham circle algorithm. In *Journal of Physics: Conference Series* (Vol. 1438, No. 1, p. 012017). IOP Publishing. (2020).

[53] Ray, B.K., 2006. An alternative approach to circle drawing. J. Indian Inst. Sci. 86 (6), 617.

[54] Bera, S., Bhowmick, P., Stelldinger, P., Bhattachary, B., 2013. On covering a digital disc with concentric circles in Z2. Theor. Comput. Sci. 506, 1–16.

[55] De Viaene, J., Derammelaere, S., Stockman, K., 2018. Load angle estimation for dynamic stepping motor motion applications. Mechatronics 53, 229–240. https://doi.org/10.1016/j.mechatronics.2018.06.017.

[56] Chase, O.A., Teles, M.B., de Jesus dos Santos Rodrigues, M., de Almeida, J.F.S., Macêdo, W.N., da Costa Junior, C.T., 2018. A low-cost, stand-alone sensory platform for monitoring extreme solar overirradiance events. Sensors 18 (8), 2685.

[57] Alsabbah, S., Mughrabi, T., 2008. Speed estimation of adaptive fuzzy-controlled piezo-electric motor using MLP-Neural Network. Am. J. Appl. Sci. 5 (11), 1518–1521. https://doi.org/10.3844/ajassp.2008.1518.1521.

[58] Alghamdi, H., Maduabuchi, C., Albaker, A., Alatawi, I., Alsenani, T.R., Alsafran, A. S., Almalaq, A., AlAqil, M., Abdelmohimen, M.A.H., Alkhedher, M., 2023. A prediction model for the performance of solar photovoltaic-thermoelectric systems utilizing various semiconductors via optimal surrogate machine learning methods. Eng. Sci. Technol. 40, 101363. https://doi.org/10.1016/j.jestch.2023.101363.

[59] Maduabuchi, C., Fagehi, H., Alatawi, I., Alkhedher, M., 2022. Predicting the optimal performance of a concentrated solar segmented variable leg thermoelectric generator using neural networks. Energies 15 (16), 6024. https://doi.org/10.3390/en15166024.

[60] Alghamdi, H., Maduabuchi, C., Yusuf, A., Al-Dahidi, S., Albaker, A., Alatawi, I., Alsenani, T.R., Alsafran, A.S., AlAqil, M., Alkhedher, M., Andiappan, V., 2023. Multiobjective optimization and machine learning algorithms for forecasting the 3e performance of a concentrated photovoltaic-thermoelectric system. Int. J. Energy Res. 2023, 1–22.